

Chapter 1

Introduction

Far infrared semiconductor detectors are desired for applications involving thermal imaging and optical signal detection. Due to the maturity of the material and processing technology, quantum well infrared photodetectors (QWIPs) had rapid development in the past 2 decades^{[1][2]}. QWIPs based on intersubband electron or hole transition. The QWIPs focal plane arrays shows promising performance. Owing to the intrinsic photoconductive type structure, QWIPs usually suffer from a higher dark current than conventional photodetectors based on band to band absorption. The special selection rule of intersubband transitions also put restrictions on the polarization of the incoming radiation.

The quantum dot infrared photodetectors (QDIPs) have been investigated widely in recently^{[3][4][5][6]}. QDIPs utilizing different structures have been demonstrated with different detection wavelength and strong normal incident response. There are some elementary differences between QWIPs and QDIPs from the experiment result. These differences come from the basic physical properties of QDs and as well as the device structure.

The frequency dependent was found both in the responsivity and noise current spectrum of QDIP. Both of their amplitude is decreased as the frequency increase. Because the similar phenomenon is shown in QWIPs and QDIPs, we studied the mechanism difference between QDIP and QWIP.

The gain of QDIP is a strong dependent on the temperature and bias. It means that the capture probability of QDs is also temperature and bias dependent. The number of carriers in QDs is considered to discuss the impact on the capture

probability. Furthermore, the impact ionization is considered to obtain the photocurrent gain. All of these works can help us to understand the characteristics in QDIP. We hope that the more deep insight of QDIP can lead us to design a QDIP which has a better performance than before.



Chapter 2

Principle

In this chapter we will focus on the operation of QDIP. First we will review the theory about the infrared radiation, and we will also introduce the characteristics and the growth of quantum dots. The photoconductor which works as the basic model of QDIP is also included in this chapter. Then we will discuss the histories and advantages of all kinds of infrared photodetectors. It is helpful for us to realize more clearly in our research topics.

2.1 Infrared radiation^[9]

Before discussing infrared photodetectors, we must realize what infrared radiation is. Infrared is an electromagnetic wave which wavelength range is between 0.7~ 1000 μ m. According to the basic theory of radiation, we knew that every object would radiate electromagnetic wave except it was under 0° K. That is the reason that why we can see the sun: the surface temperature of sun is about 6000° K and the light it radiate is located at the visible range. We could obtain the spectral density of blackbody from Planck's blackbody radiation law:

$$M(T, \lambda) = \frac{2\pi hc^2}{\lambda^5} \frac{1}{e^{hc/\lambda kT} - 1} \left(\frac{W}{m^2 \cdot m} \right) \quad (2.1)$$

$M(T, \lambda)$ is blackbody's total power under unit wavelength and unit area. C means the light velocity, h is Planck constant, k is Boltzmann constant, T is the absolute temperature of radiated object. This formula was designed for blackbody. The radiation law needs to adjust by multiplying an emissive factor of such object if the object is not a blackbody. From Eq (2.1) we can obtain Wien's displacement law:

$$\lambda_{peak} \cdot T = 3670(\mu m \cdot K) \quad (2.2)$$

We can easily prove the example that we mention previously about sun's radiation. When the object temperature is equal to the room temperature, the peak of the radiated wavelength is located around $12 \mu m$. The range of wavelength is invisible by a naked eye but for a infrared photodetector, so we can know the importance of infrared photodetectors.

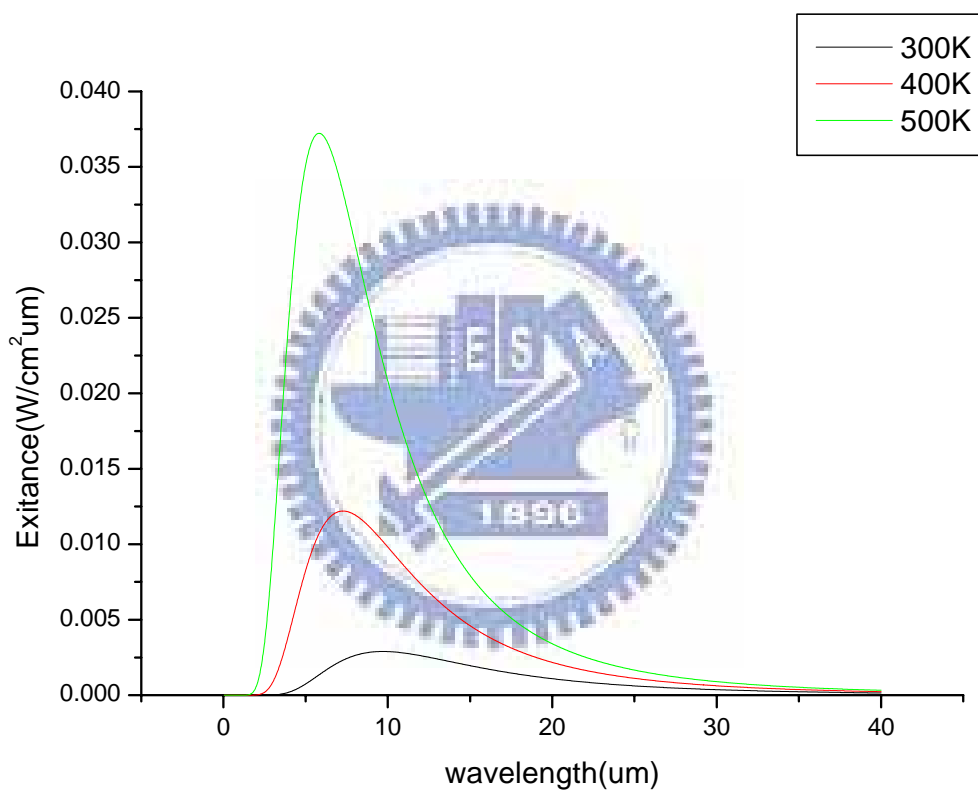


Fig 2-1 Spectral density of blackbody

Fig 2-1 are the radiation curves from Eq (2.1) at $300^\circ K$, $400^\circ K$, $500^\circ K$, and we can observe that the range of the full width of half maximum of blackbody is located around $6 \mu m \sim 17.5 \mu m$. It means that if we want to detect the infrared light which emitted by the object which have the room temperature, the best detecting range is between $5 \sim 18 \mu m$. But we still need to consider the absorption of the atmosphere in

the infrared range when we use the infrared detection. There have CO₂ and H₂O absorption in the air.

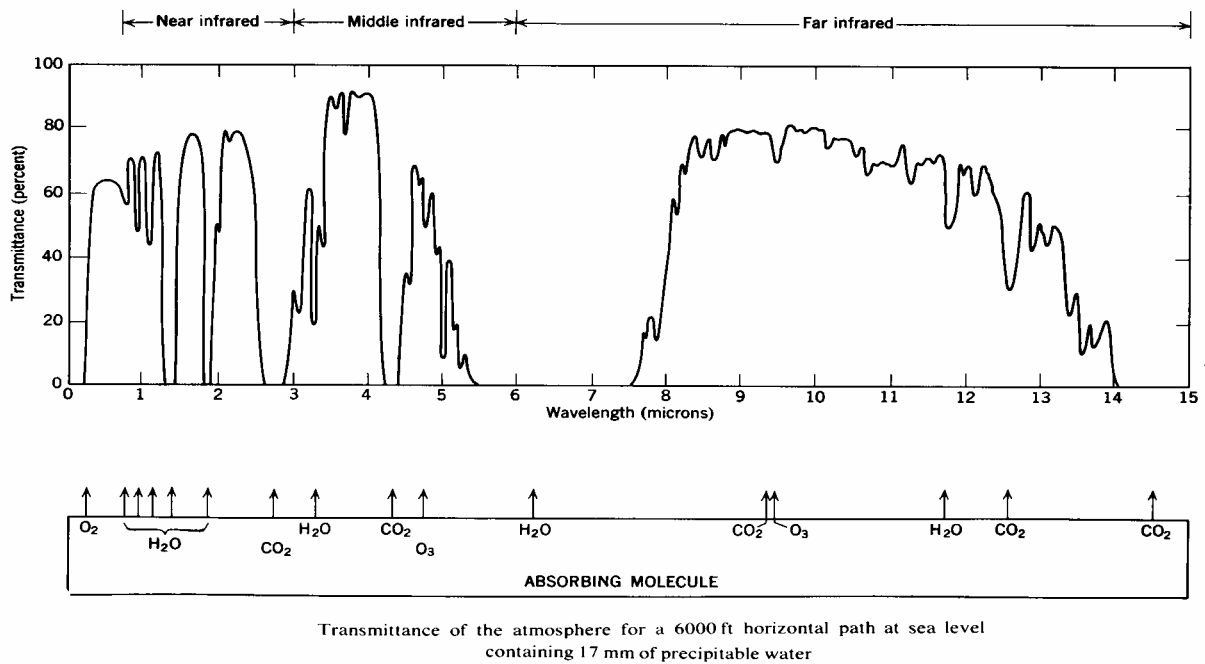


Fig 2-2 The transmission spectrum of atmosphere

2.2 The classifications of infrared photodetectors^[10]

The infrared photodetectors which have different mechanisms can be classified into two kinds: thermal detectors and photon detectors. The former one was using to detect the change of material properties because it transfers the infrared to the heat which would cause the material properties different. The latter one can absorb the infrared by electrons which cause the transition in the crystal, and we measure the current by applying a reasonable voltage. In this time, we will focus on the photon detectors.

There were two kinds of photon detectors which depended on the doping. They were intrinsic and extrinsic detectors. Now, we want to make a description about these two kinds of detectors and discuss their disadvantages. After we realize the limit about these conventional detectors, we will introduce our topic --- the development and

advantages of quantum dots infrared photodetectors.

2.2.1 Intrinsic and extrinsic infrared photodetectors

Intrinsic infrared photodetectors are fabricated by semiconductors which has no doping. The way it works is show as Fig 2-3(a). An incident photon which energy was larger than the energy gap could generate the electron-hole pair, so electrons and holes could be collected by applying a suitable voltage. The numbers of photon which could be detected were related to the energy band gap and the energy of photon. So the material which could be used as an intrinsic infrared photodetector were those who have narrow energy band gap, like (Hg, Cd) Te, (Pb, Sn) Te. We can adjust the ratio of Hg, Cd in the (Hg, Cd) Te or Pb, Sn in the (Pb, Sn) Te to get the energy bandgap we want. Because we need the detectors which can detect the wavelength between $5 \mu\text{m}$ and $18 \mu\text{m}$, the material energy gap must located from $248 \sim 68.9\text{meV}$. It was difficult to fabricate a large area matrix by using these materials, because the materials were soft when the energy gap is narrow and there also had some problems on the stability and uniformity.

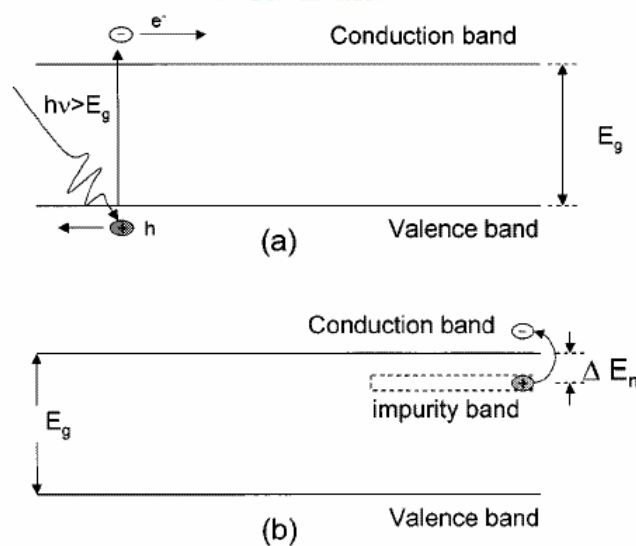


Figure 2-3 (a) intrinsic infrared photodetectors (b) extrinsic infrared photodetectors

We doped impurities into the semiconductor materials (eq. Si) which would generate the impurity level in the bandgap was the extrinsic infrared photodetectors. The energy difference between impurity state and conduction band could be used to absorb infrared. The electrons were excited from impurity level to conduction band and contributed to the photo-current. However, this kind of detectors had smaller detected range which was limited by the impurities and its material. It also could not operate at high temperature.

There has no material for infrared photodetectors that the energy level can be control exactly and easily. So, we find the way to solve this problem by using the confined energy states in quantum mechanics.

2.2.2 Quantum-Well Infrared Detectors: QWIPs

QWIPs absorbed the infrared by using electrons intersubband transition. Figure 2-4 is the theory of intersubband transition. Unipolar carrier devices are usually used as intersubband photon detectors, although it shows both the conduction band and valance band intersubband transition. Now the conduction band is considering only, the formula from the infinite deep quantum well in quantum mechanics can be presented as:

$$E_n = \frac{\hbar^2 \pi^2}{2m^* L_w^2} n^2 \quad (2.3)$$

m^* is the electron effective mass, L_w is the width of quantum well, n is a integer. The energy difference between the ground state and first excited state is:

$$E_2 - E_1 = 3\hbar^2 \pi^2 / 2m^* L_w^2 \quad (2.4)$$

These two equations are the basic ones in quantum mechanics, it implies that the energy difference between two energy states can be adjusted easily by two ways. One is change the width of the well. Another way is to choose different material to have

different effective mass. After these, we must consider that absorption is the interactions between infrared and electrons in quantum well. The impact factors include the well width, doping concentration, doping position, temperature, and the incident angle. The incident angle is the most important element in absorption. There is no absorption if the electric field of incident light is parallel to the well, which means that there is no quantity of electric field parallel to the growth direction.

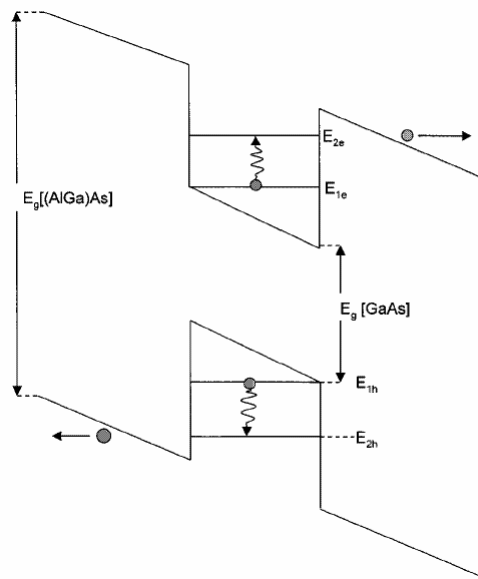


Figure2-4 Intersubband transition

QWIPs can be designed in two ways^[11]. One is bound-to-bound QWIPs which have two bound states in the same well. The electrons excited from the ground states to excited states are escaping out of the well by tunneling or thermal ionic emission. The closer the excited state to the conduction band, there are more chances for electrons to escape from the well, as shown in Fig 2-5(a). Another is bound-to-continuum QWIPs which have only one bound state in the well. The absorption occurs between the bound state and continuum state which above the conduction band. The electrons escaped out of well and contributed to photo-current only by absorbing the infrared light, as shown in Fig 2-5(b). So the escape probability of bound-to-continuum QWIPs was larger than bound-to-bound QWIPs.

Although the bound-to-continuum QWIPs have larger escape probability, the wave functions of QWIPs have less coupling. The developments of QWIPs were directed to bound-to-quasi-bound QWIPs which had a bound state very close to the edge of the well. This type of QWIPs has the better performance than the previous two cases.

Compare to the conventional detectors, QWIPs had not only mature epitaxial and processing technologies but also cost less. But the performance was limited by the large dark current and low quantum efficiency. Another problem is that normal incidence is forbidden due to the polarization selection rule. This problem can be solved by designing a grating above the device to increase the coupling of normal incidence, but for large area of array, the coupling efficiency is decreasing with the area increasing.

In order to have better performance than QWIPs, quantum dots which have 3 dimensions confined are studied recently. Quantum dots are allowed for normal incident and the dark current can be suppressed due to phonon-bottleneck. So quantum dots infrared photodetectors(QDIP) are predicted to have a better performance than QWIPs.

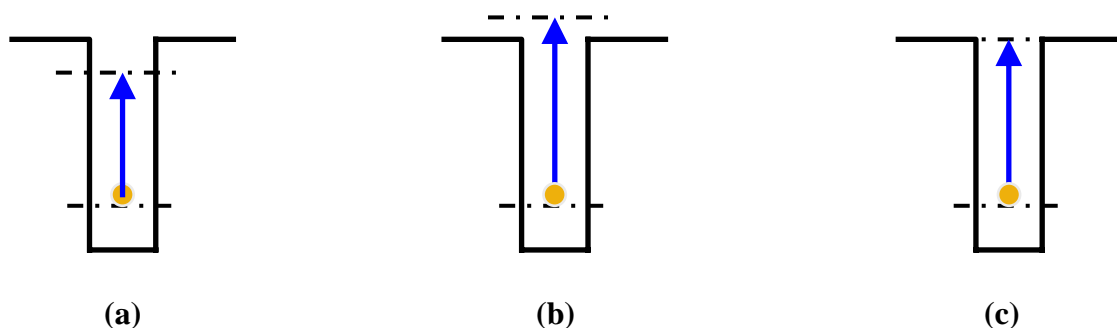


Fig 2-5 (a)Bound-to bound (b)bound-to-continuum (c) bound-to quasi-bound QWIPs

2.3 Growth and characteristics about quantum dots

2.3.1 Self Assembled QDs

The quantum dots were formed and applied to the devices in the past decade. The method to fabricate quantum dots by using lithography and etching was impractical because that the defect would lead into the structure during processing. The quantum dots were not valuable in the beginning.

Quantum dots which had a better quality were grown by molecular beam epitaxy (MBE). It was much easier to grow quantum dots by using two different materials which have different lattice constant. The upper layer material was forced by the lower layer. At the first, the material was grown in planar mode, so there formed a wetting layer. When the wetting layer reached a specific thickness, it was grown in three-dimension. This was called Stranski-Krastanow growth mode (S-K mode). The force of elastic strain relaxation would drive the quantum dots growing. Quantum dots formed only when the lattice constant misfit over than 1.7%. And the surface density was about $10^9 \sim 10^{12}$ dots/cm². In general, the shape of quantum dot is more like a pyramid than a circle.

We have some methods of measurement to realize the quality and the size of quantum dots. Atomic force microscope (AFM) can measure the density, height, uniformity, and width of quantum dots. We can realize the strain by using transmission electron microscopy. Photoluminescence and electroluminescence could verify the reality of the quantum structure. From the spectrum, we could estimate the energy level and uniformity of quantum dots. In our lab, we use InAs/GaAs material to form quantum dots.

2.3.2 Phonon Bottleneck Effect

The density of states for quantum dots structures are delta-function. Because the electron must utilize phonons to relax the energy from the excited state to ground state and the total energy of phonons must equal to the energy difference between two states, the electrons must need more relaxation time to transition between two states. It calls phonon bottleneck effect.

Phonon bottleneck effect is caused by strong quantum-confinement. Due to three dimension confinement of quantum dots, the interactions between the electrons and phonons are depressed. The relaxation time for carriers is significant slowed in quantum dots discrete levels except the phonons energy equal to the energy difference between the sublevels.

In transition theory, the relaxation time between two states was depending on the coupling of two state wave functions. The wave function of bound state was asymmetric for QD because the formation of QDs was come from the strain force caused by the lattice constant mismatch. The relaxation time from continuous state to sublevel state would be longer for QDs than quantum well. Besides, to satisfy the energy conservation rule, the transition energy between excited state and ground state must equal to the phonons energy. So electrons need longer time in QD to transition from continuous state to ground state. The electrons have longer lifetime would increase the gain of photo current. It also reduces the probability that hot carriers excite the electrons in quantum mechanics, and the dark current would be suppressed.

2.4 Photoconductor

QDIP transfers photons into current. QD is a three dimension confined which makes the energy levels quantize, so it can absorb a specified wavelength photon. The ground state electrons will be excited to higher states by absorbing a photon, then it contributes to photo-current. Because the transition occurs in the subband, the

wavelength would locate in the infrared region.

2.4.1 Noise and signal^[9]

The mechanism of photon detection is very simple. But it is complex when it applies to real devices. In this section, we review the basic theory of photoconduction, including the signal and noise. The geometry diagram is show as figure 2-6.

We defined quantum efficiency as follows:

$$\frac{\bar{n}}{\tau_d} \equiv \eta \Phi_s \left(\frac{e}{s} \right) \quad (2.5)$$

where \bar{n} is the numbers of photon which collected in τ_d second and Φ_s is the optical flux falling on a detector.

The photocurrent i_s is

$$i_s = e \frac{\bar{n}}{\tau_d} = e \eta \Phi_s \quad (2.6)$$

where e is the magnitude of an electron charge. In the generation process, including the random arrival of photons and the spontaneous response of the absorption process is assumed to be random. The process obeys Poisson distribution, based on this statistics; the mean-square fluctuation of n , also called variance is equal to the mean value:

$$\overline{(n - \bar{n})^2} = \bar{n} \quad (2.7)$$

and the mean-square fluctuation is

$$i_n^2 = \overline{(i - \bar{i})^2} = \frac{e^2}{\tau_d^2} \overline{(n - \bar{n})^2} = \frac{e^2}{\tau_d^2} \bar{n} = \frac{e}{\tau_d} i_s = \frac{e^2}{\tau_d} \eta \Phi_s \quad (2.8)$$

i_n is the intrinsic or the minimum noise current associated with optical detection. The signal power is larger than the noise power when $i_s^2 > i_n^2$, comparing Eq.(2.6) and Eq.(2.8) gives:

$$i_s^2 = e^2 \eta^2 \Phi_s^2 \geq i_n^2 = \frac{e^2}{\tau_d} \eta \Phi_s \Rightarrow \eta \Phi_s \tau_d = \bar{n} \geq 1 \quad (2.9)$$

It means that the signal is greater than the noise when more than one photoelectron is collected on the average in each sampling time. In fact, this condition is the minimum requirement to produce a DC signal. We define the noise equivalent flux Φ_{SL} to be the signal flux which equal to the level of noise:

$$NEF = \Phi_{SL} = \frac{1}{\eta\tau_d} \quad (2.10)$$

It also means that the signal noise ratio(S/N) is equal to 1. Now, we consider the photon flux addition from the background radiation Φ_b . The total noise current come from the signal and background is given as:

$$i_n^2 = \frac{e^2}{\tau_d} \eta (\Phi_s + \Phi_b) \quad (2.11)$$

and the total noise equivalent flux is

$$NEF = \frac{1}{2\eta\tau_d} + \frac{1}{2\eta\tau_d} \sqrt{1 + 4\eta\tau_d\Phi_b} = \frac{\Phi_{SL}}{2} + \frac{\Phi_{SL}}{2} \sqrt{1 + 4\frac{\Phi_b}{\Phi_{SL}}} \quad (2.12)$$

When Φ_b is larger than Φ_{SL} , the detection is background-limited.

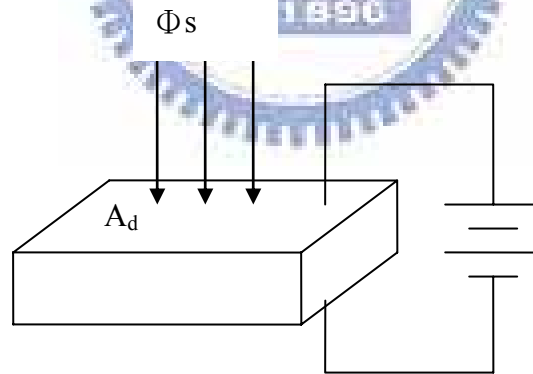


Fig 2-6 The schematic of photoconductor

2.4.2 Optical signal of a photoconductor

An optical flux Φ_s incident normally into a device has the surface area A_d as shown in Fig.2-6. Due to the absorption by device, the intensity of the incident light decreases with the penetrating depth x .

$$\Phi(x) = \Phi_s (1 - r) e^{-\alpha x} \quad (2.13)$$

where r is the reflective factor of detector surface, α is the absorption coefficient. In the steady state, the electron density is independent with time:

$$\frac{\partial \rho(x)}{\partial t} = G(x) - \frac{\rho(x)}{\tau} = 0 \quad (2.14)$$

where τ is the recombination lifetime and G is the generation rate given as:

$$G(x) = -\frac{1}{A_d} \frac{d\Phi(x)}{dx} \quad (2.15)$$

so we can derive the average photoelectron density $\bar{\rho}$:

$$\bar{\rho} = \frac{1}{L} \int_0^L G(x) dx = \left[(1-r) \alpha \int_0^L e^{-\alpha x} dx \right] \frac{1}{A_d L} \Phi_s \tau = \eta \frac{\Phi_s \tau}{A_d L} \quad (2.16)$$

When we apply a voltage, the photo current i_s will be:

$$i_s = A_d \bar{\rho} e v_d = A_d \left(\eta \frac{\Phi_s \tau}{A_d L} \right) e (\mu F) = \eta \Phi_s e \left(\frac{\mu F \tau}{L} \right) = \eta \Phi_s e g \quad (2.17)$$

where v_d is the drift velocity of electrons, μ is the mobility, F is the electric field. We can easily realize the photoconductor gain g by defining $g = \mu F \tau / L$. g can be present as the times a electron passes the sample. Because electron has a finite lifetime, each one can only complete part of the circuit before recombination, so we choose the effective charge in a photoconductor.

2.4.3 Dark current

Dark current is an important mechanism because it affects the performance of QDIPs. The dark current can be divided into two parts. One is n-i-n diode current, show in Fig 2-7(a), which do not pass through the QDs, the other part is come from the QDs. There are several possible ways that the dark current can be generated in the QDs. First, the current which contributed by the carriers ionized to the continuum states by thermals is called thermal ionic current, shown in Fig 2-7(b). This kind of

current is exponential to the temperature, so this is the main part of dark current when the temperature is higher than 50K. The second is thermally assisted tunneling current which show as Fig 2-7(c). The carriers are excited to the higher state which is still lower than the barrier, but the thermals help the carriers to tunnel through the barrier which becomes a part of dark current. Both of these two currents are smaller in QDIPs than QWIPs due to the phonon-bottleneck effect. And the third is direct tunneling current which independent of temperature. It is contributed by the carriers in the QDs which direct tunnel the barrier, and it can be reduced by increasing the barrier width.

In order to get a better performance, we cap a layer of AlGaAs which have a higher energy gap than the QDs to suppress the dark current. This layer is growth between the QDs to block the current pass through the QD region where has the lower energy gap. In other words, it increases the n-i-n resistant by reducing the effective area.

Sometimes we doped in our device to increase our photocurrent. But the position and the total quantity of doping are very important in our devices. For example, if the doping position can not push the carriers move into the QDs, or the doping is too much for the QDs, then the carriers will contributed to the leakage current.

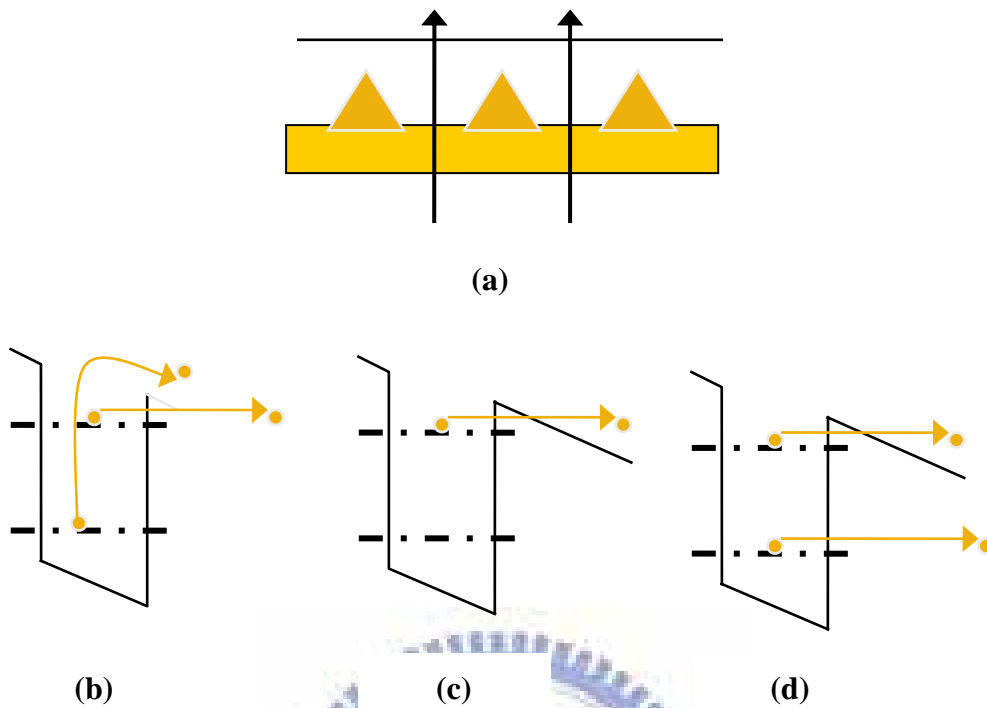


Fig 2-7 (a) n-i-n diode effect (b)thermionic emission (c)thermal assisted tunneling (d)directly tunneling

2.4.4 Noise

The performance of QDIP is also determined by the signal to noise ratio. Although the noise associated with each physical mechanism has a specific name, the basic mechanics of noise can be classified into two parts, the fluctuation in the velocity, for example, Johnson noise. The other one is the fluctuation in the number of the carriers, for example, generation-recombination (g-r) noise.

Johnson noise can be stated as follows

$$i_n = \sqrt{\frac{4kTB}{R}} \quad (2.18)$$

which k is Boltzman constant, R is the resistance of the detector, B is the bandwidth.

For g-r noise, there are $\bar{n} = \eta\Phi_s$ light absorption events in every second, each event produces an effective charge ge. It can be present as,

$$i_n^2 = \frac{g^2 e^2}{\tau_d^2} n = \frac{ge}{\tau_d} I = 2geIB \quad (2.19)$$

I is the total current generated by optical excitation and thermal excitation. In the random recombination process, g is the average value of the gain when an electron recombines at time τ which is the average lifetime of a photoelectron or a thermal electron. Due to the recombination process, the fluctuation of g would increase the noise power by a factor 2. The total noise current can be stated as

$$i_n^2 = 4egIB \quad (2.20)$$

The device gain can be known by using

$$g = \frac{i_n^2}{4eI} \quad (2.21)$$

There still have some other noises should be consider in it, for example, the noise caused by impurity states, tunneling current and leakage current. In order to have a better performance, flicker noise (1/f noise) and the outer circuit noise also need to take into account.

2.4.5 Detectivity and BLIP condition

NEF has discussed in section 2.4.1, and the definition of NEP (noise equivalent power) is the signal power that equal to the total noise power. NEP also can be presented as the product of NEF and photon energy. Because the NEP is proportional to $\sqrt{A_d B}$, it is more convenient to compare with other detectors by defining the detectivity D^* as follows,

$$D^* = \frac{\sqrt{A_d B}}{NEP} \quad (2.22)$$

Now, the total current we consider is

$$I = i_s + i_b + i_{th} = \eta ge \left(\Phi_s + \Phi_b + \frac{i_{th}}{\eta ge} \right) \quad (2.23)$$

which i_s is the signal current, i_b is the background noise, and i_{th} is the thermal noise.

So the S/N ratio can be stated as

$$(S/N) = \frac{i_s^2}{i_n^2} = \frac{(\eta g e \Phi_s)^2}{4 g e I B} = \frac{\eta}{4 B} \frac{\Phi_s^2}{\Phi_s + \Phi_b + \frac{i_{th}}{\eta g e}} \quad (2.24)$$

Now we consider the detection which is signal limited, so the noise equivalent flux Φ_{SL} will be

$$\Phi_{SL} = \frac{4B}{\eta} \quad (2.25)$$

this flux is a factor of two larger than eq(2.10) which gain is constant($g=1$). We will discuss it more detail in chapter 4.

2.4.6 Focal plane Array

It is very important for detectors to apply in the focal plane array by using readout integrated circuit. Indium ball is used to connect the pixel and the readout circuit. Each pixel receives the photocurrent and stores it in the capacitance when it applies a bias. The signal in the capacitance is sampled and transferred to the image signal. The important parameter to realize the uniformity of the array is noise equivalent temperature $NE\Delta T$,

$$NE\Delta T = \frac{NEP}{\frac{dP_b}{dT} \sin^2\left(\frac{\theta}{2}\right)} = \frac{\sqrt{AB}}{D_b^* \left(\frac{dP_b}{dT}\right) \sin^2\left(\frac{\theta}{2}\right)} \quad (2.26)$$

which D_b^* is the detectivity of the blackbody radiation. $NE\Delta T$ means the temperature resolution of the detectors. Due to the mature growth and process technologies in group III-V which makes it possible to have a high uniformity array.

Chapter3

Process

3.1 The growth of device

3.1.1 epitaxy

The samples were grown by molecular beam epitaxy(MBE) machine which could control the growth exactly in heterostructures. 5000 Å buffer layer was grown on (100) GaAs semi-insulating substrate to lower the surface defect of substrate. Ten period of InAs/GaAs QDs with 500 Å barriers which grown by using Stranski-Krastnow mode were used in the active region. Each period consisted 470 Å GaAs layer and 30Å Al_{0.2}Ga_{0.8}As current blocking layer. The total active region consisted ten QDs layers and eleven barrier layers which was sandwiched by 5000 Å n-type contact layer. δ -doped Si layer with concentration of $1 \times 10^{10} \text{ cm}^{-2}$ was inserted 20 Å before each QD layer to supply carriers into QDs. The nominal thickness of InAs QD is 2.6ML. The schematic figure is shown in figure3-1.

3.1.2 Straski-Krastanow growth mode

There are three modes for thin film growth^[12]. When the surface energy of thin film surface is smaller than the substrate, the thin film will grow layer by layer, which is called Frank-van der Merwe (FM) mode, as Fig.3-3(a). The second is Volmer-Weber (VM) mode; it will grow as a 3D island when the surface energy of thin film is larger than substrate, as Fig 3-3(b). The third is Stranski-Krastanow (SK) mode. In the beginning of epitaxy, the surface energy of the thin film is smaller than substrate, so it grows layer by layer in 2D. Because the surface energy increases with

the epitaxy thickness, it grows as an island when it reach a specified thickness, as shown in Fig 3-3(c). Our samples are grow in S-K mode. The material we use, for example, InAs forms above the substrate in 2D layer in first 2ML. After it, InAs will grow as islands, as shown in Fig 3-4.

The way to fabricate QDs by photolithography and etching had a poor quality because it caused serious damage to the crystal during the etching process. Self-assembling is a novel way to fabricate quantum dots, for example, dislocation-free and high density coherent islands of InAs are self-assembled on the GaAs substrate. It provides a good optical performance in the device application.

3.2 process

Standard processing techniques were used to define mesa and make ohmic contacts. First, we defined the mesa via photolithography and wet etching. The sulfate based etching solution is used with the concentration as H_2O_2 : H_2SO_4 : H_2O = 1: 8: 40. The etching rate is about 200Å/s. During the process, the etching rate is confirmed by the α -stepper. Each mesa is etched to the bottom contact region. The size of the mesa are 1.23×10^{-3} and 3.36×10^{-4} cm², and the size of the window are 2.25×10^{-4} and 4.52×10^{-4} cm². The contact metal was defined after the mesa process.

The ohmic metal consists of Ni/Ge/Au (300 Å / 700 Å / 2000 Å). It was deposited by E-gun. After lift-off, the sample is annealed under inert ambiance by RTA (400°C, 20sec) to form a good ohmic contact. Finally, the connections to the grounds and mesa tops was done by wire bonding for the following measurement.

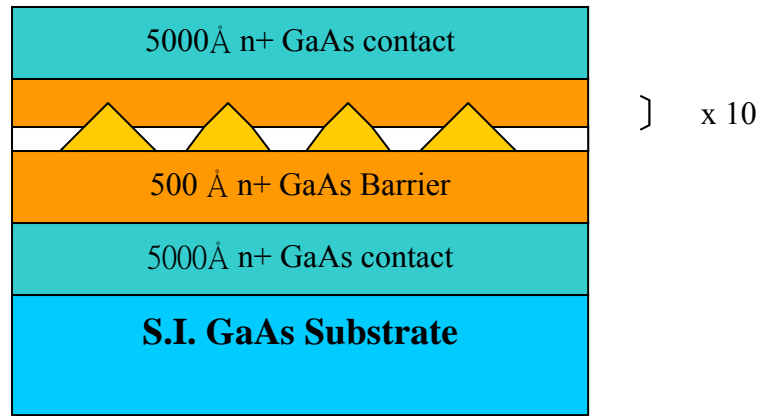


Fig 3-1 Structure of QDIP

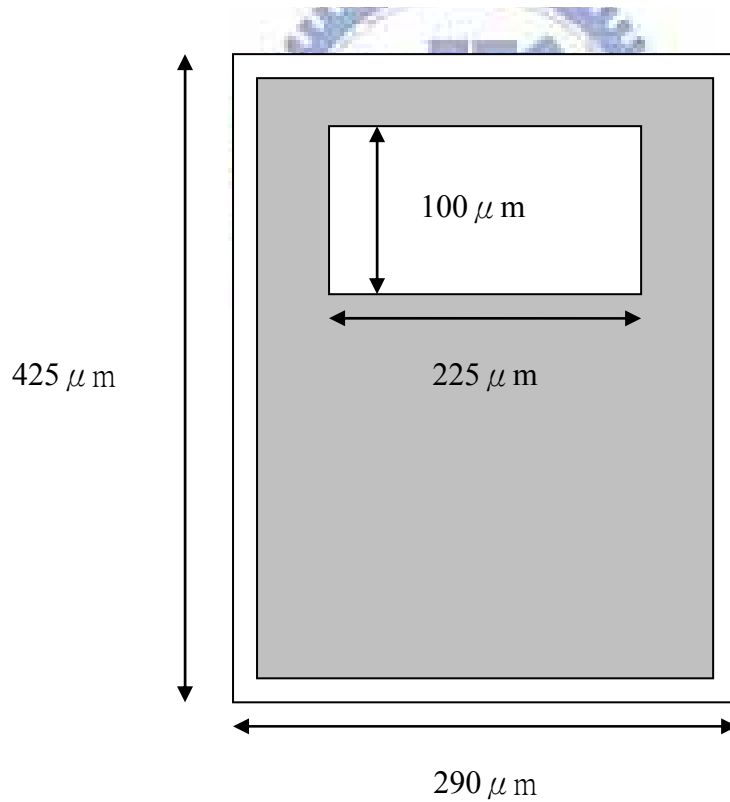


Fig 3-2(a) The shape of mesa and window

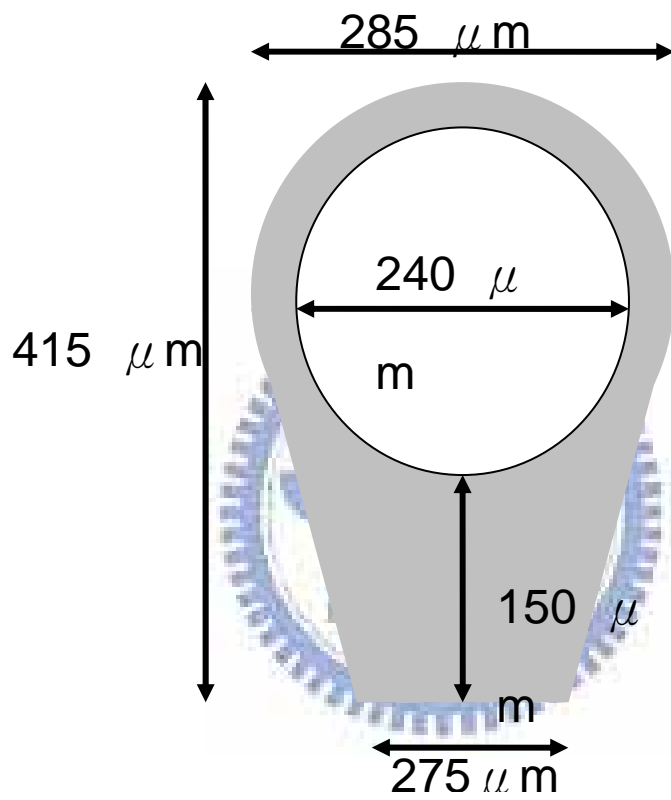
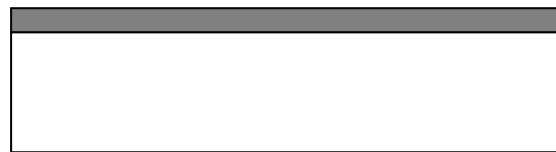
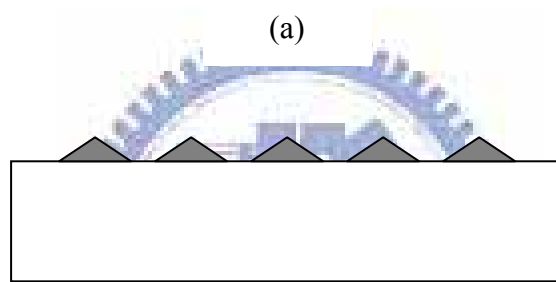


Fig 3-2(b) The shape of mesa and window



(a)

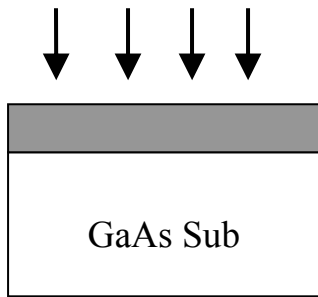


(b)

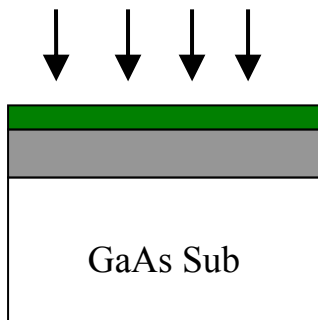


(c)

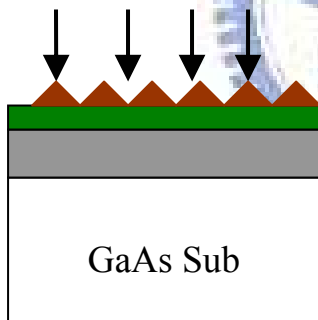
Fig 3-3 (a) Frank-van der Merwe(FM) mode (b)Volmer-Weber(VM) mode (c)Stranski-Krastanow(SK) mode



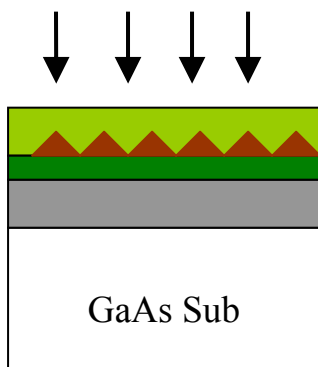
(a) grow buffer layer to lower the defect on the substrate surface.



(b) In the beginning, the surface energy of InAs is lower than the substrate, it grows in 2D layer by layer.



(c) When the InAs was reached 2.6ML, the strain energy caused the surface energy larger than substrate, and quantum dots was formed to released the energy.



(d) The AlGaAs layer was capped on the InAs quantum dots to blocking the dark current.

Fig 3-4 S-K mode

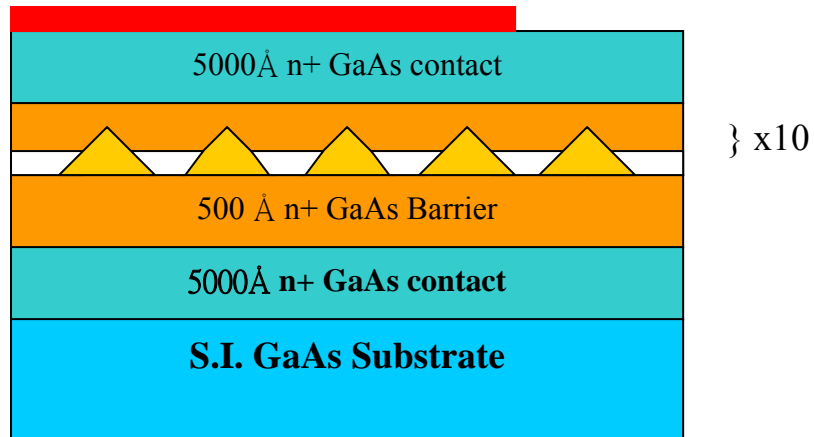


Fig 3-5(a) Define the mesa region with P.R.

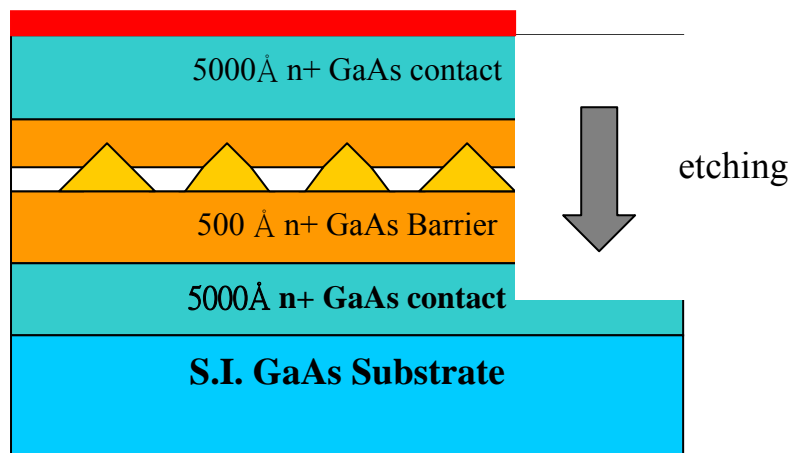


Fig 3-5(b) Etching to bottom contact layer(H_2O_2 : H_2SO_4 : H_2O = 1: 8: 40)

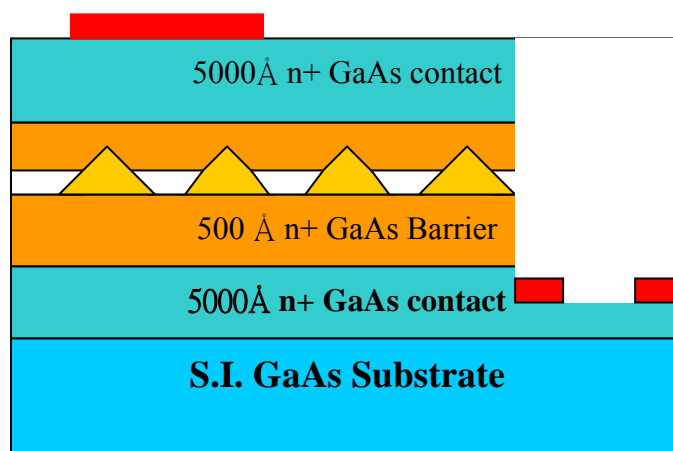


Fig 3-5(c) Define metallization region with P.R.

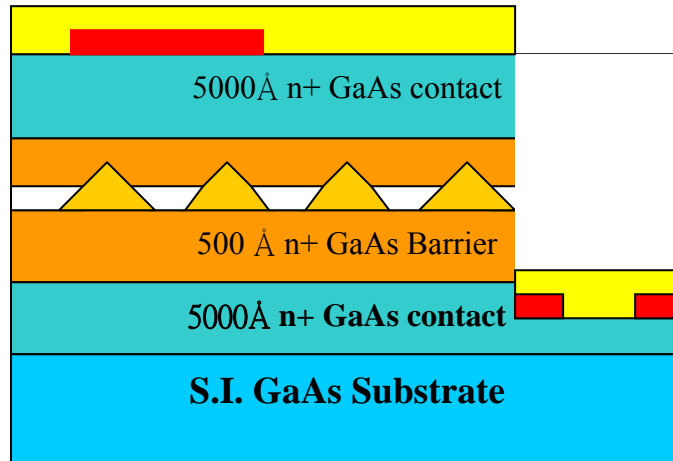


Fig 3-5(d) Evaporate contact layer by E-gun(Ni/ Ge/ Au= 300/700/2000Å)

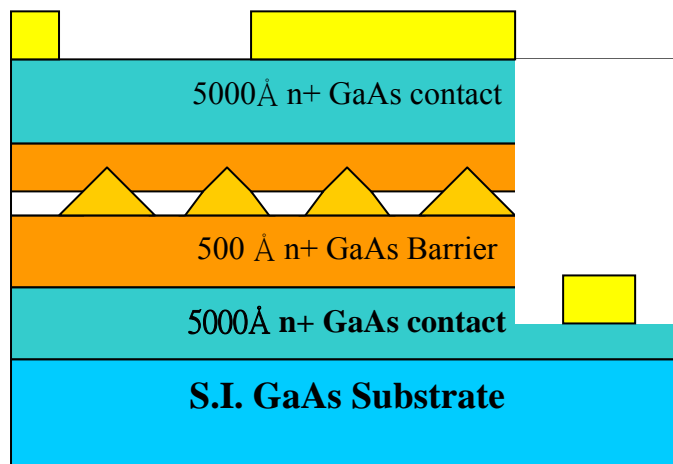


Fig 3-5(e) Lift-off P.R. and RTA

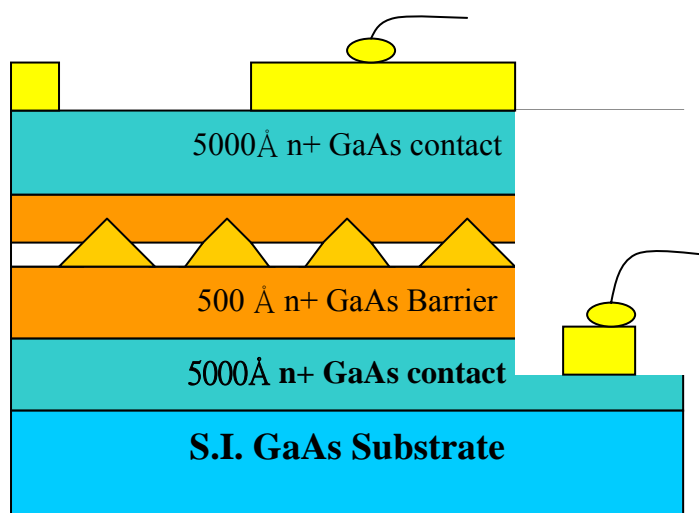


Fig 3-5(f) Wire bonding for cryogenic measurement

Chapter 4

Measurement Principle and Instrument Setup

Before processing, the quality of samples must be checked first by photoluminescence (PL) and atomic force microscope (AFM). After it, we perform the detector characterization, such as measure the responsivity, dark current, spectrum, noise analysis and background limited performance condition.

4.1 Photoluminescence (PL)

PL has been widely used in III-V semiconductors to investigate the optical characteristics. The basic theory is pumping high energy photons (larger than the energy gap) into samples to generate the electron-hole pairs, then the photons emitting is measured during the e-h pairs band to band recombination. The PL system in our laboratory includes a Triax-320 monochromator, Argon-ion pumping Laser, optical chopper, SRS530 lock-in amplifier, cryogenic pump and Si-detector. The whole system was shown in Fig 4-1.

In high temperature, the carriers will distributed in higher states and the probability of non-radiative recombination will also increase. In order to have a clear signal, the sample was cooling down closed to liquid helium temperature (4.2K). From the PL, the confined states of QDs can be confirmed. The uniformity of QDs can be determined from its full-width-half-maximum.

4.2 Atomic force microscope

Atomic force microscope is a powerful tool to investigate the surface

morphology of the samples. Therefore, the density, size and distribution of the grown QDs are characterized by AFM. In our experiments, the doping concentration in the QDIP is determined by the measured data. The higher doping concentration would lead to current leakage. In contrast, the lower doping concentration would decrease the photocurrent.

4.3 Fourier Transform Infrared Spectrometer (FTIR)

Spectrometers measure the absorption intensities of the sample at the certain range of frequency. The key component to FTIR is Michelson interferometer. The configuration is shown in Fig 4-2. The signal from the detector is sent to a computer and converted into an IR spectrum through a Fourier transform.

Due to the selection rule, normal incident light cannot be absorbed by quantum well structure. The transition rate between states is:

$$W_{i \rightarrow f} = \frac{1}{h} \sum_f \left| \langle f | H_{\text{int}} | i \rangle \right|^2 \delta(E_f - E_i - hf) \quad H_{\text{int}} = p \cdot E \quad (4.1)$$

E_f and E_i are final state and initial state, E is the electric field, and p is the polarization vector. From the eq(4.1), the light can be absorbed only when the electric field is parallel to the z-direction. For QDs, the incident light absorption is allowed because of its 3D confinement structure.

4.4 Responsivity^{[1][13]}

The detector has different response under different wavelength. In other words, for different frequency, the detector generates different photocurrent even if the light intensity is the same. The QDIP spectral response $R(\lambda)$ is measured in infrared region via FTIR. But $R(\lambda)$ is the relative value. In order to analyze the QDIP more clearly, the spectral response is normalized at the peak wavelength λ_p response. Then

normalized response spectral $\tilde{R}(\lambda)$ was used to calculate the peak responsivity R_p . It is shown in following:

$$R(\lambda) = R_p \cdot \tilde{R}(\lambda) \quad (4.2)$$

Blackbody is the source of the photons. The radiation power $M(\lambda)$ is shown in eq(2.1). The total power per unit wavelength of blackbody which incident into the detectors is shown as below:

$$Q(\lambda) = A \cdot T_{ZnSe} \cdot T_{GaAs} \cdot T_{Ge} \cdot MF \cdot E \cdot M(\lambda) \quad (4.3)$$

$$E = \frac{(d/2)^2}{D^2 + (d/2)^2} \quad (4.4)$$

which A is the detector area set by the window size, T_{ZnSe} , T_{GaAs} , T_{Ge} are the transmission factors of the lens; MF is the modulation factor of chopper, E is the projected solid angle, d is the aperture diameter of blackbody, D is the distance from the detector to the aperture.

In our experiment, the temperature of the blackbody was 1273K, the aperture size is 0.2 inch, and the distance between device and blackbody is 15cm. The transmission factor of T_{ZnSe} , T_{GaAs} , T_{Ge} are 0.7, 0.64, 0.74 and the modulation factor of chopper is 0.38. The Ge filter is used to block the photons which wavelength is lower than 2um because those photons generate the interband transition photocurrent. The electrons which excited by the incident photons are measured by the lock-in amplifier, so even under low bias the signal can still be measured.

The relation between the photocurrent and incident photons is shown in following:

$$I_p = \int_{\lambda_1}^{\lambda_2} R(\lambda) Q(\lambda) d\lambda = R_p \int_{\lambda_1}^{\lambda_2} \tilde{R}(\lambda) Q(\lambda) d\lambda \quad (4.5)$$

the parameters in $Q(\lambda)$ were shown in eq(4.3). We can obtain the peak responsivity R_p by measuring I_p and $\tilde{R}(\lambda)$. The photocurrent is dependent on the temperature and bias, so the R_p also varies with the bias and temperature. The setup system is shown in figure4-3.

4.5 Dark current and Background photocurrent

The theory of dark current is described in chapter2. The configuration of the experiment setup is shown in Fig4-4. The setup difference between the background photocurrent and dark current is that the heat shielding of cryostat is closed for blocking the background radiance.

4.6 Noise analysis

The performance of a QDIP not only depends on the responsivity, but also depends on its noise current. It is determined by the signal noise ration(S/N). The noise current can be classified into two parts, one is dark current noise, and the other is 300K background photocurrent noise. The photoconductive gain is obtained by measuring the dark current noise only, because the dark current gain and photocurrent gain are difficult to measure separately.

The main components of dark current noise are thermal noise, generation-recombination, and Flicker (1/f) noise.

Thermal noise, also called Johnson noise, is existed in all material with resistance. The random motion of carrier caused thermal noise. It is shown as follows:

$$i_n^2 = \frac{4kT}{R} B \quad (4.6)$$

k is a Boltzmann constant, T is the temperature of resistance, R is the resistance value, B is the bandwidth.

Flicker noise is inverse proportional to the frequency. This term is important when the device operates at low frequency. For most semiconductors, Flicker noise is related to its surface effect.

The fluctuation of the carrier density caused by the generation and recombination of the free carriers is called generation-recombination noise. The noise current is:

$$i_n = 2I \left[\frac{\tau B}{N_0 (1 + \omega^2 \tau^2)} \right]^{1/2} \quad (4.8)$$

where τ_d is the lifetime of free carriers, N_0 is the number of free carriers in the device, and it also the number of electrons which transition from the ground states to excited states. The current is governed by $I = qn_0/\tau_d$, τ_d is the time for electron to travel through the device. The noise current was:

$$I_n = (4qIg \frac{B}{1 + \omega^2 \tau^2})^{1/2} \quad (4.9)$$

g was defined as the gain of the device, the G-R noise is:

$$I_n = \sqrt{4qIgB} \quad (4.10)$$

In QDIP, the noise current is contributed by the electron trapping in and escaping from QDs. The dark current gain is almost the same as photocurrent gain in QDIP although they had different mechanisms.

The experiment setup is shown in Fig 4-5. The noise current of device is sent into SR-570 amplifier, and then measures by SR-770 network analyzer. The noise spectrum is measured under different bias. The total noise is shown as follows:

$$i_n^2 = i_{Johnson}^2 + i_{n,G-R}^2 + i_{n,1/f}^2 \quad (4.11)$$

Because the G-R noise should be separated from the total noise current, we must eliminate the thermal noise and Flicker noise by subtracting the zero bias noise. The formula is shown in following:

$$V_n^2 = V_{n0}^2 + A^2 I_n^2 \quad (4.12)$$

V_n is the noise at a specify bias, V_{n0} is the noise at zero bias, A is the amplify of SR-570. The gain of QDIP is shown as follow:

$$g = \frac{I_{n,G-R}^2}{4qI_d} \quad (4.13)$$

4.7 Detectvity

D^* is a measure of single detector sensitivity because the power signal to noise ratio of a measurement is proportional to D^* :

$$\left(\frac{S}{N}\right)_p = (D^* I_0)^2 A 2\tau_d \quad (4.14)$$

τ_d is the integration time in the measurement. So a detector with a large D^* will have a higher S/N. The specific detectivity D^* of a single detector is defined as:

$$D^* = \frac{R\sqrt{A_d B}}{i_n} \quad (4.15)$$

where R is the responsivity, A_d is the detector area, B is the measurement noise bandwidth and i_n is the noise current. Under the normal thermal imaging condition, J_{tot} includes both the dark current density J_d and the 300K background photocurrent density J_p . The background photocurrent noise is:

$$i_{nb} = \sqrt{4eg i_b B} = \sqrt{4eg(R)P_b B} = \sqrt{4e^2 g^2 B \left(\frac{\eta P_b}{h\omega}\right)} \quad (4.16)$$

where P_b is the background incident power. BLIP (Background Limited Performance Condition), ie $J_p > J_d$, is important in thermal imaging because it indicates the robustness of the system against other possible noise sources. For example, if J_d is larger than J_p , a small non-uniformity in J_d will cause a large fixed pattern noise in the FPA image, and it is the noise source expected to be dominate at a long integration time. If the device is operate under BLIP, the D^* is:

$$D_{BLIP} = \frac{1}{2} \left(\frac{\eta A_D}{\hbar \omega P_b} \right) \propto \sqrt{\eta} \quad (4.17)$$

From the eq(4.17), the D_{BLIP} depends only on quantum efficiency and the photon irradiance level.



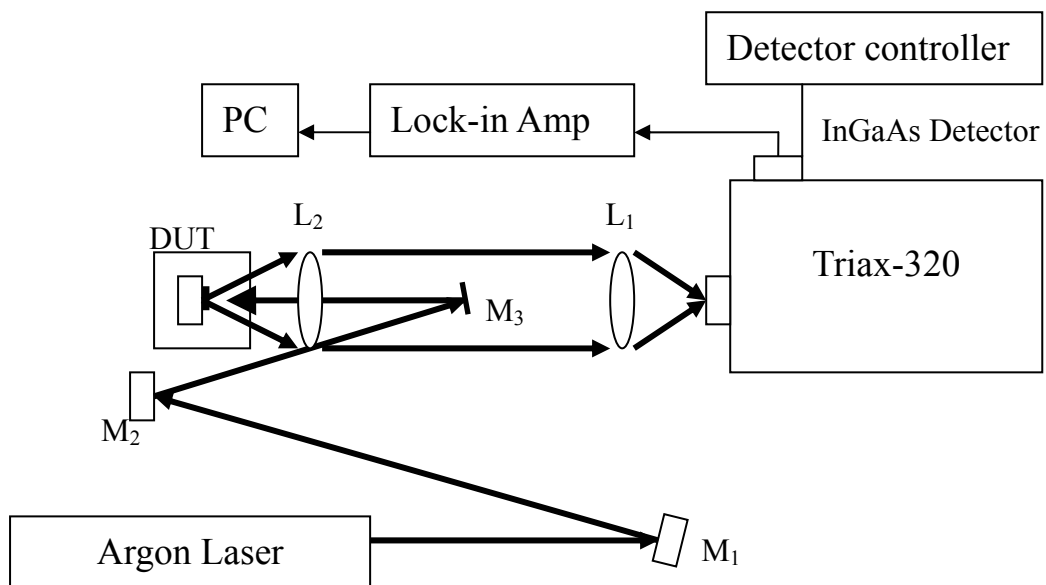


Fig 4-1 Schematic of PL system

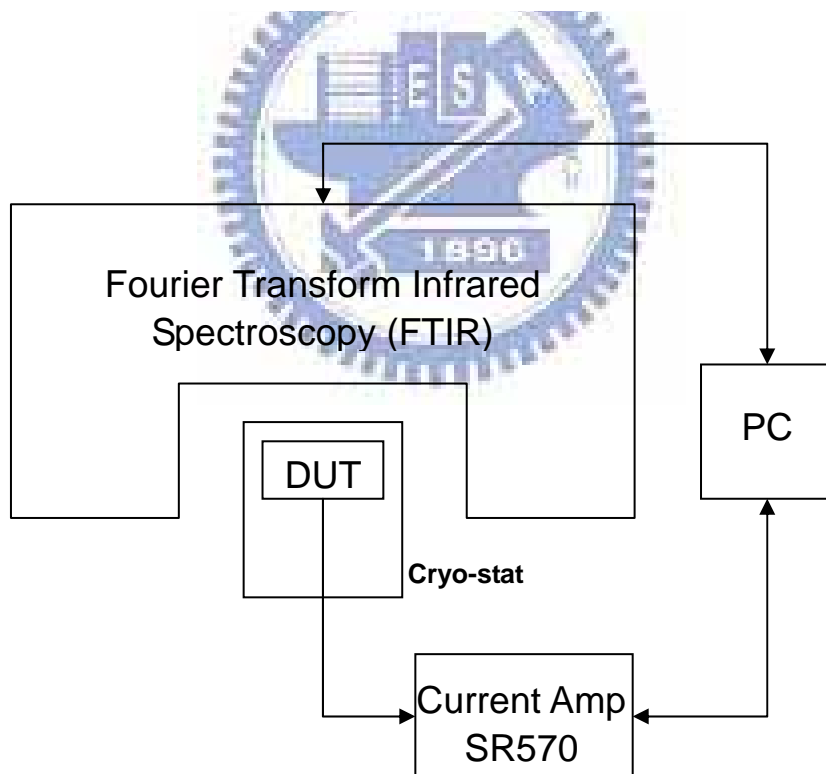


Fig 4-2 The setup of FTIR

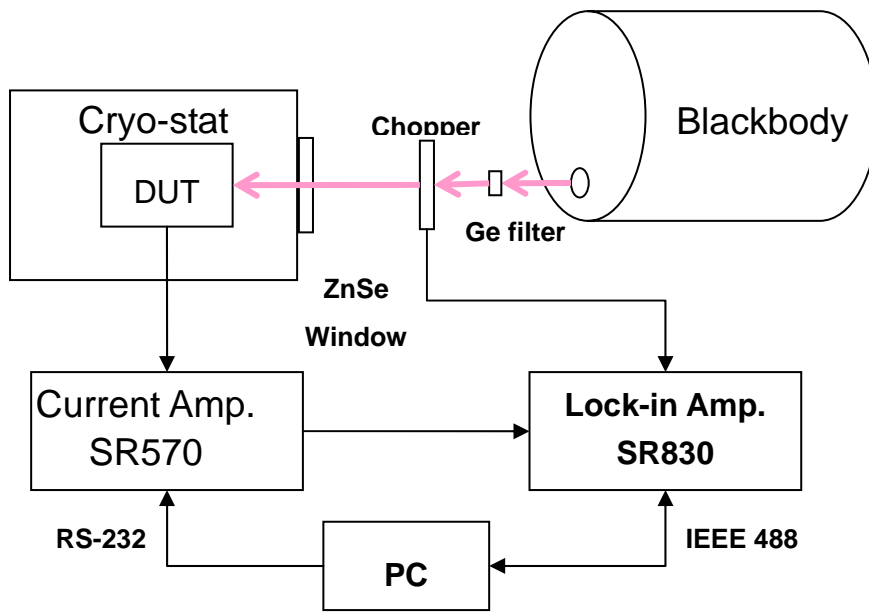


Fig 4-3 photo-current measurement set-up

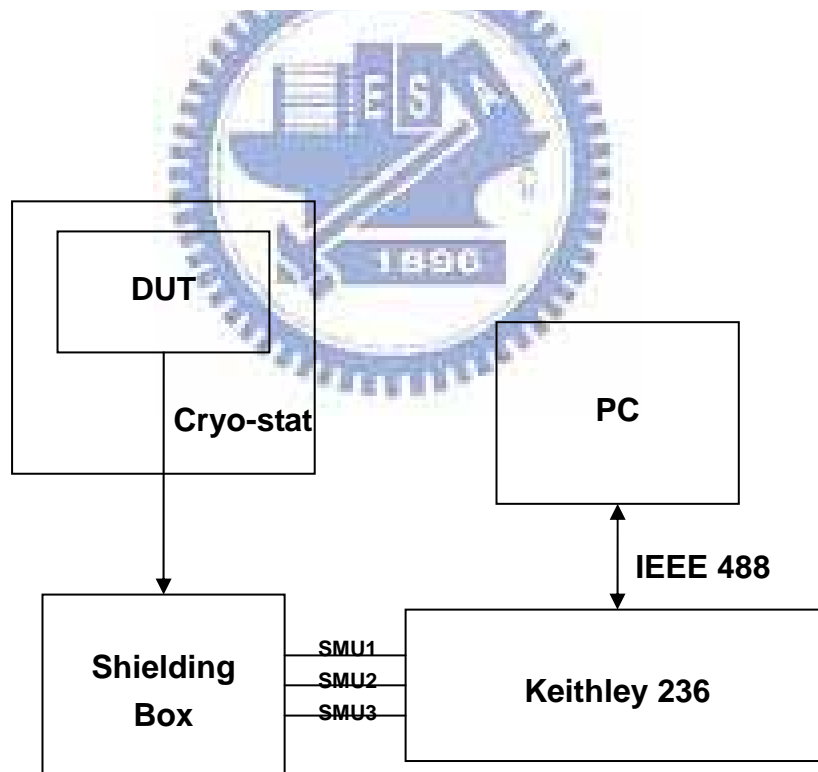


Fig 4-4 Dark current measurement set-up

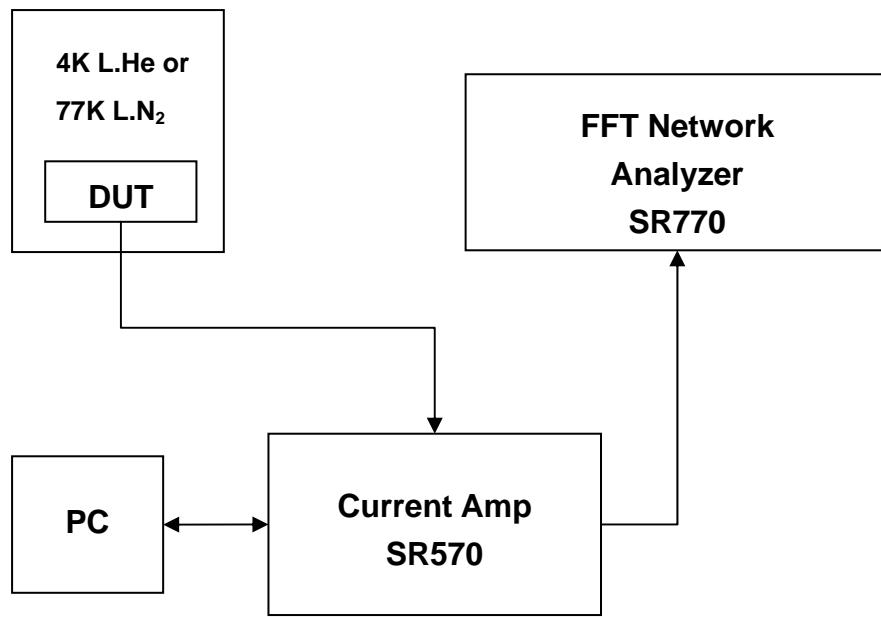


Fig 4-5 Noise measurement Set-up



Chapter 5

Results and Discussion

It is observed that the amplitude of dark current noise and photo response were frequency dependent in QDIPs in very low frequency range. Also, the responsivity is not stable with the temperature change. The transient phenomenon was discovered in QWIP. In order to realize the carrier transient difference in QDIP and QWIP, the transient model of QWIP was introduced to explain the carrier's behavior. The responsivity change was investigated with the current gain and the capture probability.

Two samples A and B we used were grown by MBE on a (100)-oriented semi insulating GaAs substrate. The 500nm Si-doped GaAs were used for top and bottom contacts. 10 periods of InAs QDs and GaAs barrier layers formed the active region. For the sample A, 50nm GaAs barrier is used and the active region was sandwiched by two 22nm $\text{Al}_{0.2}\text{Ga}_{0.8}\text{As}$ blocking layers. For the sample B, each QD is cover by 3nm $\text{Al}_{0.2}\text{Ga}_{0.8}\text{As}$ layer and 117 nm GaAs barrier. From the AFM measurement, the dots density of both samples was around $2.8\text{E}10 \text{ cm}^{-2}$. The dot height was 6nm, and the width was 26nm. The schematic of the samples were shown in Fig 5-1 and Fig 5-2.

5.1 Frequency Photo-Response

The frequency dependent behavior was analyzed by the chopper and lock-in amplifier system with blackbody as well as the FFT noise spectro-analyzer. The chopper provided the photo response from 30Hz to 3500Hz. The samples were inserted into a liquid He or liquid N_2 dewar to provide a temperature variable and low noise environment, and G-R noise is assumed to dominate the noise at low bias region.

The analyzer could provide the frequency dependent signal to 100KHz. However, the low frequency signal in the noise spectrum is dominated by $1/f$ noise, and is neglected in the results.

The frequency response measurements with 1000°C blackbody for different biases and temperature were shown in the Fig 5-3 and Fig 5-4. As these plots showed, the response was not entirely flat but decayed with increasing frequency. The cut-off frequency increases as bias or temperature increase. It is obvious the photocurrent decayed with frequency at 40K while the response is almost flat in 90K. The same behavior happened when the bias increased from 0.4V to 1.1V at 60K. In addition to the photo response, the dark current noise also showed similar trend. Fig 5-5 showed the noise spectrum from the FFT noise analyzer. This confirms the dark current and photocurrent in QDIPs have similar transport mechanism. Such a transient behavior is not welcome in high speed applications and similar phenomenon has been observed in QWIP. However, the published transient time for QWIPs is around $1 \mu\text{s}$ which is much shorter than what we observed. In order to analyze the problem, the analytical mode proposed for QWIP was used. The model was proposed by M. Ershov et. al. in 1999 and will be discussed in the next section.

5.1.1 Analytical model of transient photoresponse^[7]

The band diagram of QWIP in this model is shown in Fig 5-6. The active region comprises QWs, separated by the AlGaAs barriers. The active region is sandwiched between the doped emitter and collector contacts. When bias applied, carriers excited from the QWs due to either thermionic emission or photoemission traveled toward the contact. These carriers could be captured into the QWs or collected by the collector. In the other hand, the electrons injected from the emitter contact could compensate the space charge and keep the continuity of the current. The carriers generated from the

QWs and the current injected from the contacts are the two component of the total current and have different frequency responses.

The fast component is caused by carriers which are excited and emitted from the quantum wells as shown in Fig 5-7(a). During the fast transient and before the start of the slow transient, the electric field in a QWIP is “frozen”, the contact layer stops the excess carriers for the QW recharging. It means that the contact layer provides no excess electrons injection.

This photoemission of carriers leads to the formation of a space charge region within the active layer. During the slow transient, the QWs are recharged, and the electric field at the injection contact is increased to induce extra injection, so that the transient photocurrent is increased to reach its steady-state.

From the model, the transient photocurrent in response to a photon flux step is:

$$I(\omega) = I_{ss} \left(\frac{1}{1+i\omega\tau_c} \left\{ 1 - \frac{g}{1+i\omega\tau_c} \times \left[1 - \exp\left(-\frac{1+i\omega\tau_c}{g}\right) \right] \right\} + \frac{1}{1+i\omega\tau_0} [1 - \xi(g)] \right) \quad (5.1)$$

where g is the gain of QWIP, τ_c is the capture time of QWs.

$$\xi(g) = 1 - g(1 - e^{-1/g}) \quad (5.2)$$

$$\tau_0 = \frac{\varepsilon}{\gamma_e \xi(g)} \quad (5.3)$$

where $\gamma_e = \partial j_e / \partial E_e$ is the differential conductivity of the emitter barrier. The real part and imaginary of numerator in eq(5.5) are:

$$\text{Re} = \left(1 - g + g \cdot e^{-1/g} \cos\left(\frac{\omega\tau_c}{g}\right) - \omega^2 \tau_0 \tau_c + \omega \tau_0 g e^{-1/g} \sin\left(\frac{\omega\tau_c}{g}\right) \right) + (1 - \xi)(1 - \omega^2 \tau_c^2) \quad (5.4)$$

$$\text{Im} = \left(\omega \tau_c - g e^{-1/g} \sin\left(\frac{\omega\tau_c}{g}\right) + \omega \tau_0 - \omega \tau_0 g + \omega \tau_0 g e^{-1/g} \cos\left(\frac{\omega\tau_c}{g}\right) \right) + (1 - \xi) \cdot 2\omega \tau_c$$

The plot of frequency response has a two flat and two falloff regions as show in Fig 5-9. The first falloff is caused by the cutoff of the slow transient current, which is the

injection current from the emitter. The second is due to the carrier emission effect. The flat region between two falloff regions is under the nonequilibrium operation regime.

The amplitude of the two components also depends on the parameters of the device. When the gain is large, the ratio between the fast component I_{fs} and the total current is:

$$I_{fs} = I_{ss} \xi(g) \approx \frac{1}{2g} \quad \text{if } g \gg 1 \quad (5.5)$$

where I_{ss} is the total current. It is clear that the ratio of high frequency component decreased with bias.

5.1.2 Fitting in QDIP

The gain of QDIP is shown in Fig 5-8. It increases with the bias and saturated when bias reaches certain level. For QDIP, the gain is much higher than in QWIPs. In typical QWIPs, the gain is around 0.2 for AlGaAs/GaAs system. The amplitude of the fast component is thus much smaller in QDIP. It is shown clearly in Fig 5-3 that the response ratio for the total current and the fast component large than 10 under certain circumstances. The high gain also results in the low cutoff frequency in QDIPs. It is consistent with eq (5.3), the time constant will increase when gain gets higher.

The fitting curve of responsivity is shown in Fig 5-10. Due to the limitation of the chopper speed, the second flat region at higher frequency cannot be observed. But the first cutoff region is quite similar with this model. Fig 5-11 is the fitting of the noise current. For the low frequency the noise current is dominated by the flicker noise, which is much higher than other frequency. The frequency dependent is clear for frequency higher than 100Hz. From this plot, the slopes between two curves are slightly different, this phenomenon also occurs in responsivity presented in Fig 5-10.

The time constant τ_0 is inverse proportional to the first cutoff frequency. It is

compared with the responsivity and noise current at the same temperature is shown in Fig5-12(a). Noise current has larger τ_0 than responsivity. For photo response, the background photocurrent will have lower resistance than that of the dark current, which caused the decrease in τ_0 .

From the analysis, there still have some difference between QWIP and QDIP. The time constant τ_0 is one order larger in our experiment than in the model. It is due to that the frequency region we extract the gain is high. So we use the gain at low frequency where have a larger noise current region is shown in Fig 5-12(b). It shows a good agreement with our experiment result. Although there still have some inaccuracies to apply this model in QDIP, the trend between them is quite similar.

5.2 The temperature dependent of QDIP

In QWIPs, it has been confirmed that the photo response in most devices are temperature independent. However, the measurements of responsivity in QDIP were not the same. As shown in Fig 5-13, the responsivity shows clear temperature dependence. In order to investigate this problem, a thick barrier sample B was used in the section to provide better voltage resolution.

For the responsivity, it increases with the bias and saturated when bias reach a certain level. The responsivity also increased as the temperature increased, but the saturation voltage is less at high temperature. In order to understand this behavior, current gain is calculated from the noise current measurement. The formula we used is:

$$i_n^2 = 4qI_d g_n \quad (5.7)$$

where i_n is the noise current, I_d is the dark current, and g_n is the gain of the dark current. G-R noise is assumed to dominate the noise source at low bias region.

Because photocurrent has the similar transport mechanism with the dark current, the gain of photocurrent g_{ph} is almost the same with the dark current gain. The noise current spectrum for different bias and temperature are shown in Fig 5-16 and Fig 5-17. The frequency dependent of noise current has been discussed in previous section. Using eq(5.7), the noise gain under different bias and temperature is shown in Fig 5-15. Due to the limitation of the measurement system, the background and circuit noise are dominant when the noise current is lower than $1E-12 \text{ A/Hz}^{1/2}$. So, for lower temperature, the noise current is available only at high bias. The quantum efficiency can be obtained by using the formula:

$$\eta = \frac{R}{\frac{e}{h\nu} \cdot g_{ph}} \quad (5.8)$$

where η is the quantum efficiency, R is the peak responsivity. Fig 5-18 shows the quantum efficiency using the obtained noise gain. This is not the true quantum efficiency, because this gain has impact ionization under high bias and we will discuss it later.

5.2.1 Carrier number in QDs

The current gain shows the similar trend as the responsivity. It means that the carrier transport dominates the photo response behavior. According to Pauli's principle, the finite number of states inside QDs will decrease the capture probability when more carriers are in the QDs. $\langle N_k \rangle$ is assumed as the average excess number of carriers in QDs. The capture probability p_k into QDs has been proposed as ^[6]:

$$P_k = P_0 \frac{N_{QD} - \langle N_k \rangle}{N_{QD}} \exp\left(-\frac{e^2 \langle N_k \rangle}{Ck_B T}\right) \quad (5.9)$$

$$C \cong \left(\frac{2\epsilon\alpha_{QD}}{\pi\sqrt{\pi}} \right)$$

N_{QD} is the number of maximum excess carriers that can occupy each QD, K_B is the Boltzmann constant, p_0 is the capture probability for QDs, which have the average number of carriers, ϵ is the dielectric constant, and a_{QD} is the lateral size of QDs. It is clear that as the number of electrons increases the p_k decreases exponentially. At a given $\langle N_k \rangle$, p_k increases with the temperature increasing, which is shown in Fig 5-19(a), (b).

Assuming the capture probability in each QD layer is the same, the gain can be approximated as $g_0 = 1/N * p_k$, where $N=10$ is the number of the QDs layers. The calculated p_k of sample B at difference bias and temperature is shown in Fig 5-20. It shows that $\langle N_k \rangle$ increases as the bias or temperature increase. It means that as the current increase, the number of excess carriers in QDs will increase. This phenomenon can be explained by considering the balance of electron number in QDs. The number of carriers captured by the QDs is $N_c = j * p_k$. In Fig.5-20, the number of captured carriers increases with bias at 60K from 0.5V to 1.2V. Because the number of carriers emit out of QDs must equal to the number of carriers captured in the QDs, $\langle N_k \rangle$ will increase to enhance the excited carrier number. Thus, the carrier number will increase with voltage under the same temperature. At a given bias, the capture probability is increase with the temperature if $\langle N_k \rangle$ is constant in Fig 5-19(b). From the Fig 5-21, the capture probability decreased with the temperature in our experiment. It means that the more $\langle N_k \rangle$ must exist in the QDs in higher temperature to decrease the capture probability. When the temperature gets higher, more carriers will be emitted from the QDs. More carriers must be captured to balance this lost.

5.2.2 Impact ionization

When the bias is low, the excited carriers have to overcome the barrier to become photocurrent. As the bias increase, the escape probability will increase and reach 1 under certain bias. But from Fig 5-18, the ratio of responsivity to the noise gain decreases rapidly when the bias further increases. It implies some other effect happened at high bias range to enlarge the noise. As we know, when the kinetic energy of carriers increases, impact ionization may happen if the kinetic energy of the carriers exceeds the activation energy of the trapped carrier. The comparison between E_k and activation energy (E_a) is shown in Fig 5-22. It is clear that $E_k > E_a$ when the bias is higher than -1.2V and 1.3V. These two voltage is very close the onset of the slope change of the gain curve. When impact ionization happens, the relation between the gain and the noise current is^[8]:

$$i_n^2 = 2eg_{ph}I_d\Delta f\left(2M - p_c\left(2M - 2 + \frac{1}{M}\right)\right) \quad (5.10)$$

where M is the multiplication factor, defined as the ratio between the signal with and without impact ionization. The approximation of the equation when $p_c \ll 1$ is:

$$i_n^2 = 4eg_{ph}I_d\Delta fM \quad (5.11)$$

If we assume that the ratio of responsivity to the noise gain, which is the quantum efficiency keeps constant, shown in Fig 5-23, after the E_k is larger than E_a . So the gain without impact ionization could be obtained, which is photocurrent gain, as shown in Fig 5-24 and the multiplication factor M is determined from eq(5.11) and also shows in Fig 5-25. It is clear that the multiplication increases fast with biases, especially at low temperature. It could be more than 100 if the temperature is low enough. For high temperature curve, since the dark current is high, the measurement range is not as large as the low temperature ones. The M is close to one. It is noticed that some curves are not monotonic with voltage. That might due to that our criteria for the onset voltage is very rough. When the temperature is high, the average kinetic energy might be higher and the onset voltage is lower than our estimation. This might be the reason that the curve is not quite reasonable. Besides, the large current under high temperature will increase the scattering in the current and the probability for impact ionization decreases.

5.3 Conclusion

The transient of carriers in QDIP cause the strong dependent on frequency. In order to have correct physical elements such as quantum efficiency, and the detectivity, the frequency dependent must be separated. The two components of photo response, fast transient and slow transient, give us the idea that the transport in QDIP and QWIP are quite similar. It helps us to understand the transient mechanisms in QDIP more

clearly.

Many groups had studied the temperature dependent of QDIP. Gain also shows the dependent with temperature. For the analysis, the model is used to calculate the number of excess carriers in QDs because the excess carriers will stop the capture of the carrier. From this model, the number of excess carriers is obtained under different bias and temperature. It shows that the excess carriers increased with the current. The possible explanation of this is that the higher current would cause more carriers captured into QDs.

The gain of QDIP increases with bias is much stronger than QWIP. Impact ionization is expected when the kinetic energy of carriers is larger than the activation energy. Because the capture probability is $\ll 1$ in QDIP, we can obtained the approximation between the noise current, multiplication factor and photocurrent gain. Then the multiplication factor can be obtained.

From the above, some basic mechanisms in QDIP are realized, and the deep insight of QDIP could be obtained. The phenomenon we discussed here is favorable in real applications. The study here is helpful to the new device structure that do not have serious slow transient current and temperature stable responsivity.

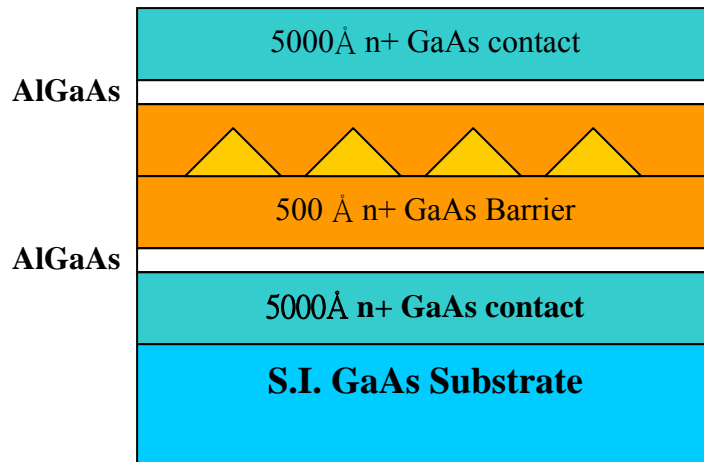


Fig 5-1 The schematic of sample A

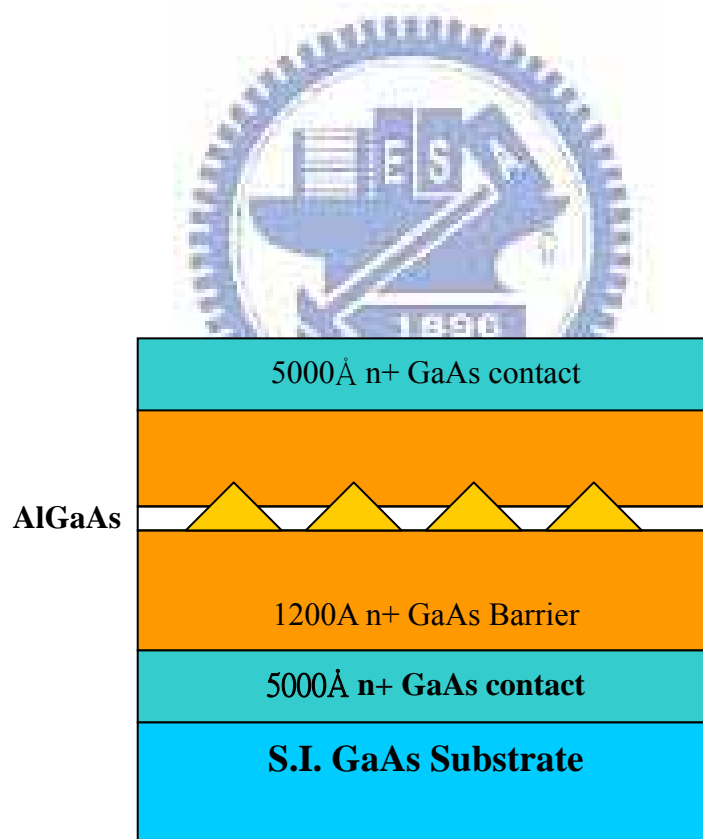


Fig 5-2 The schematic of sample B

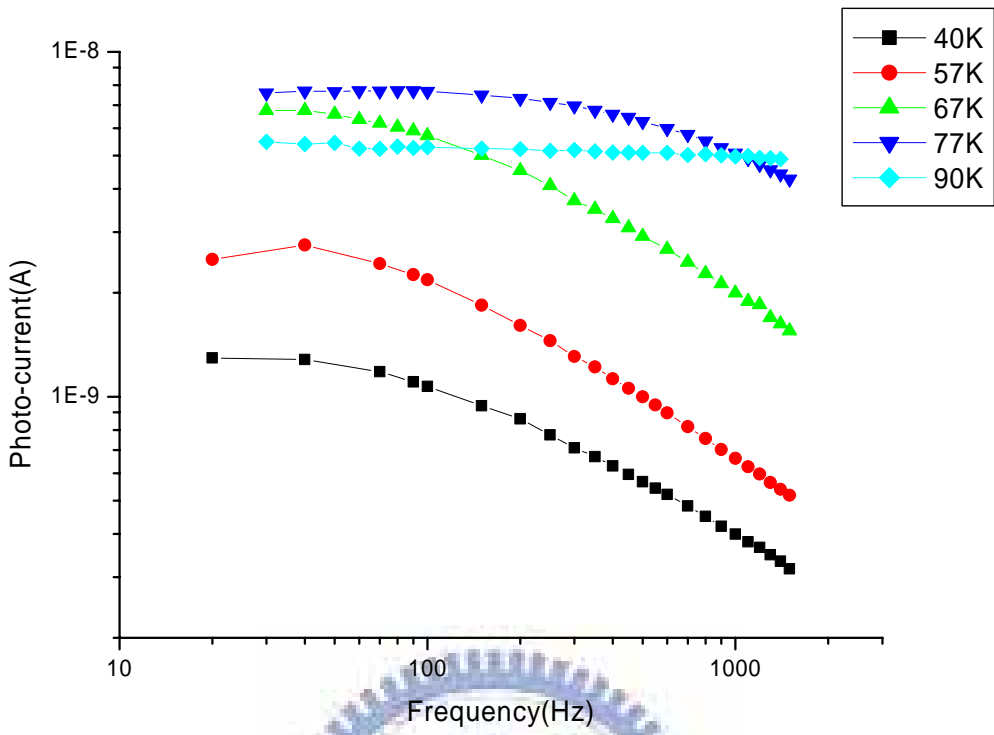


Fig 5-3 Frequency response at 1V

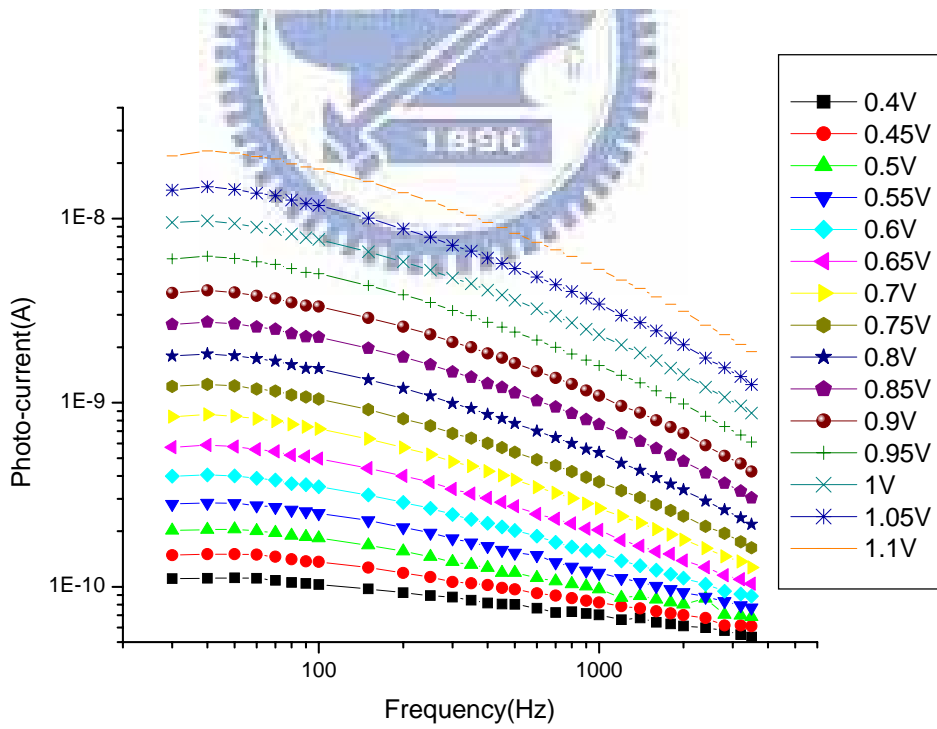


Fig 5-4(a) Frequency response at 40K

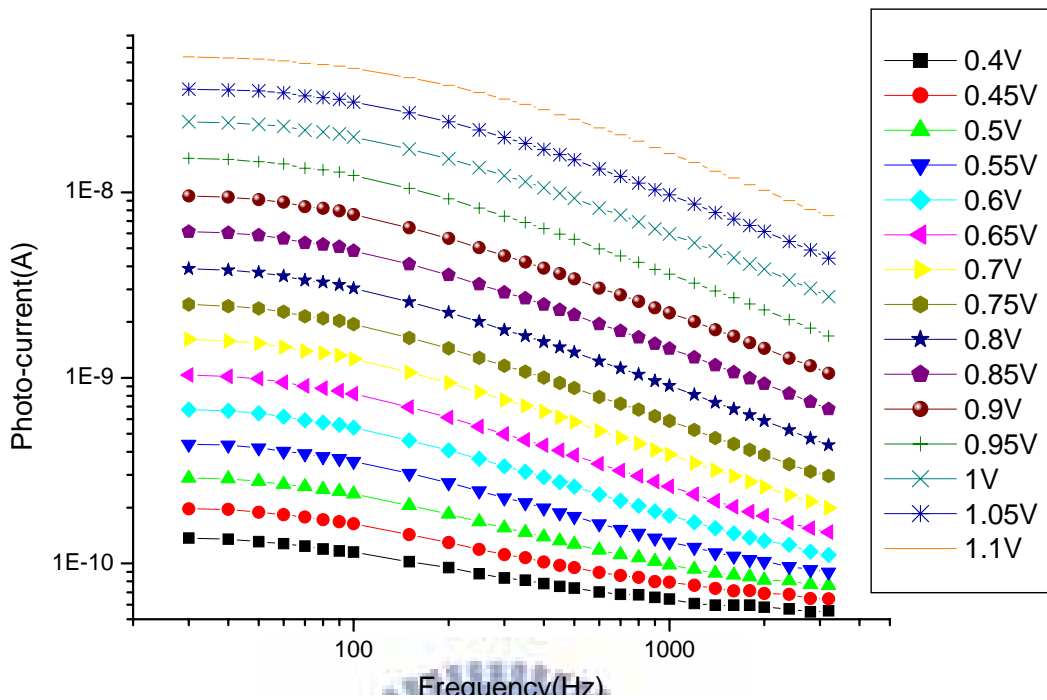


Fig 5-4(b) Frequency response at 50K

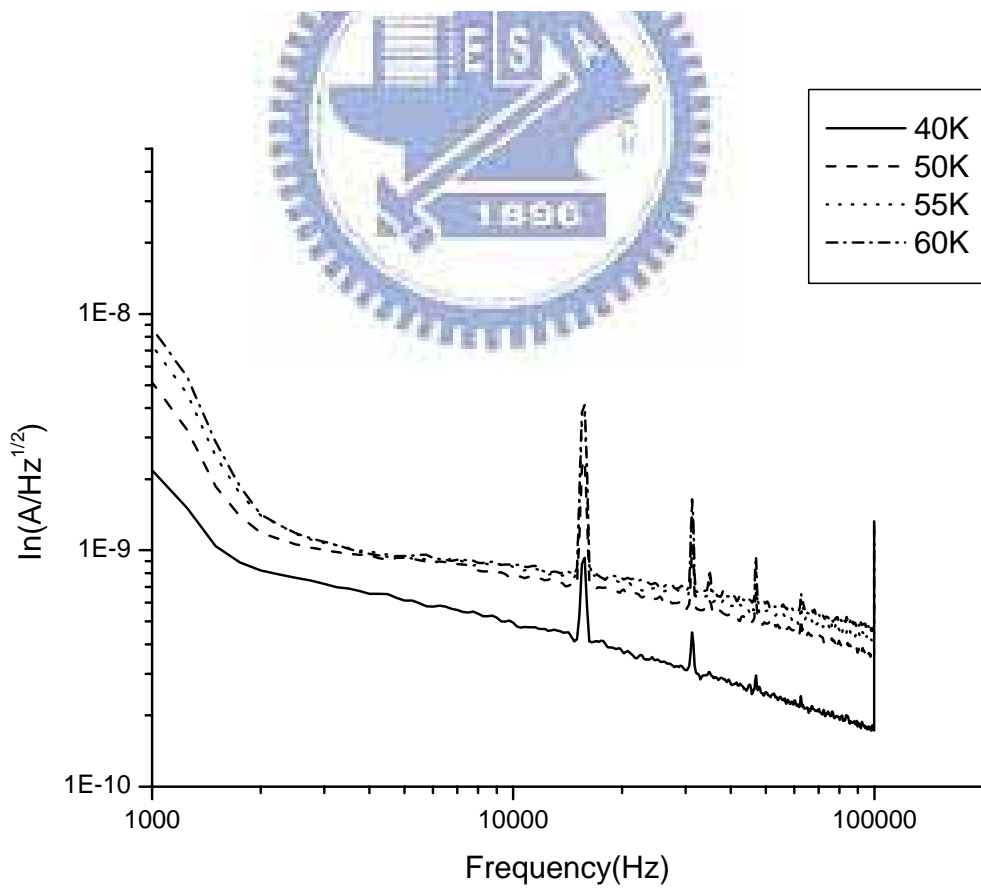


Fig 5-5 (a) Noise current at 1.4V

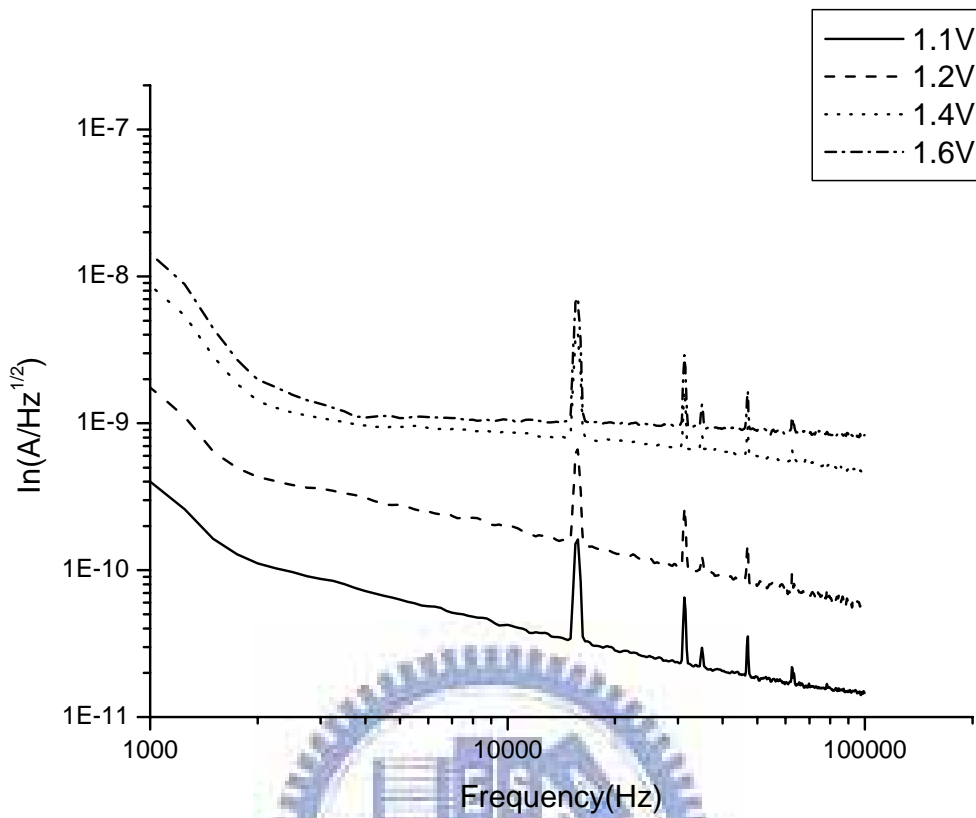


Fig 5-5 (b) Noise current at 77V

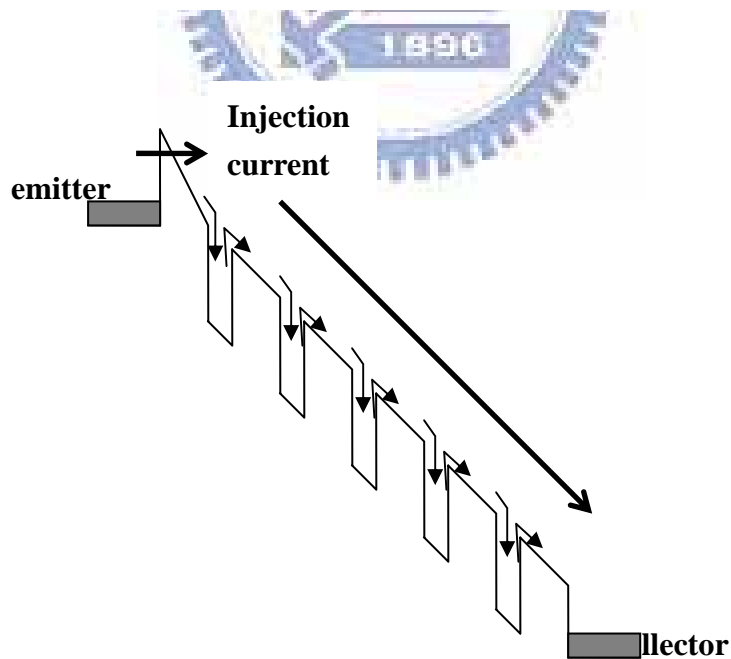


Fig 5-6 The band diagram of QDIP

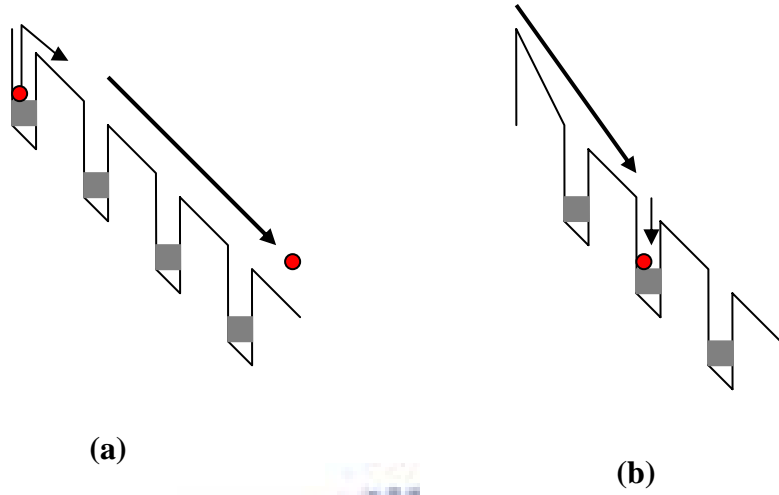


Fig 5-7 The schematic of a (a) fast (b) slow current transient

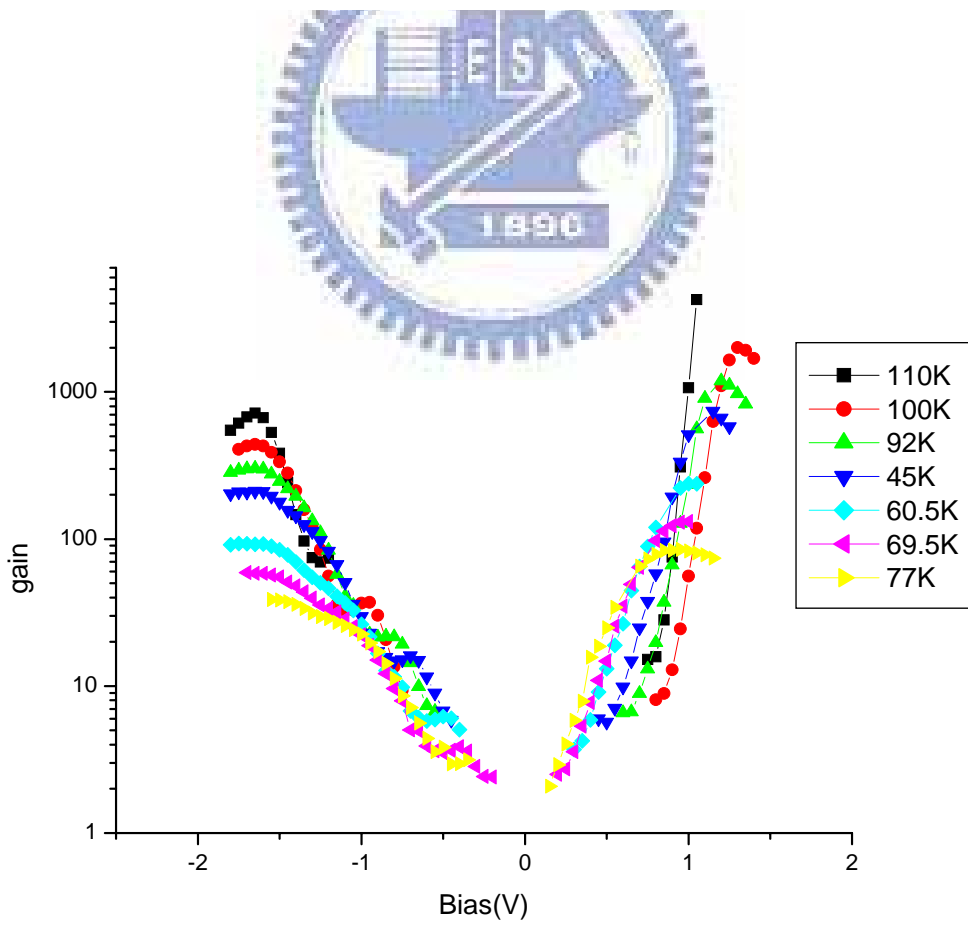


Fig 5-8 Noise gain for different temperature

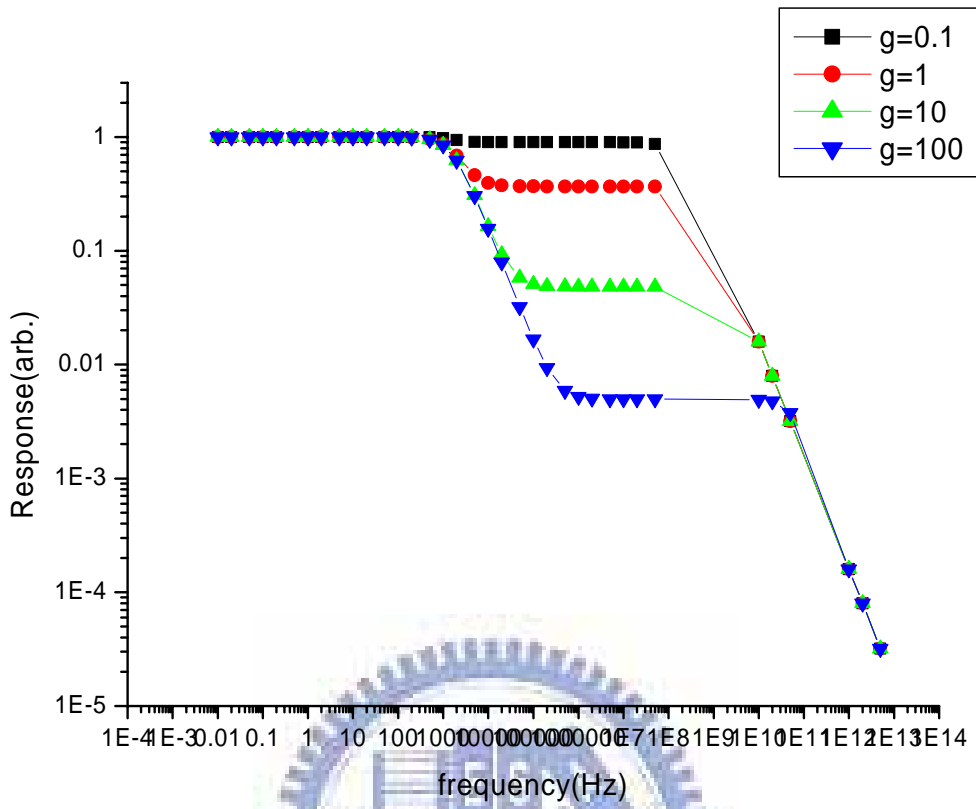


Fig 5-9 60K frequency response at different bias

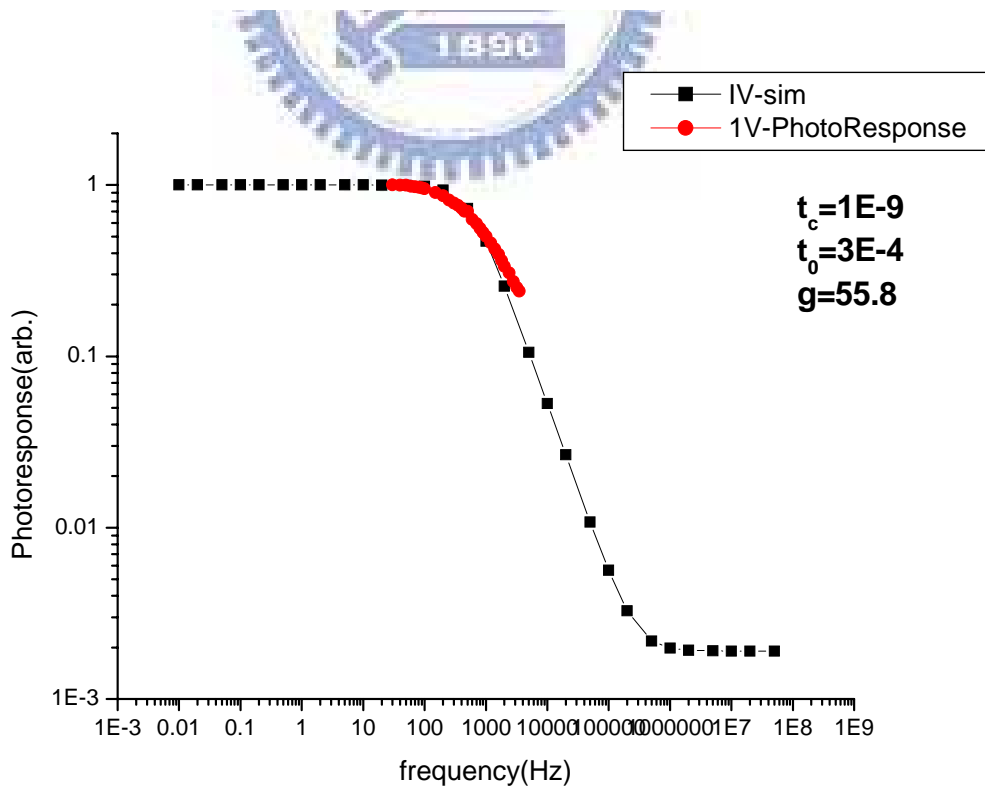


Fig 5-10 The response fitting under 60K, 1V

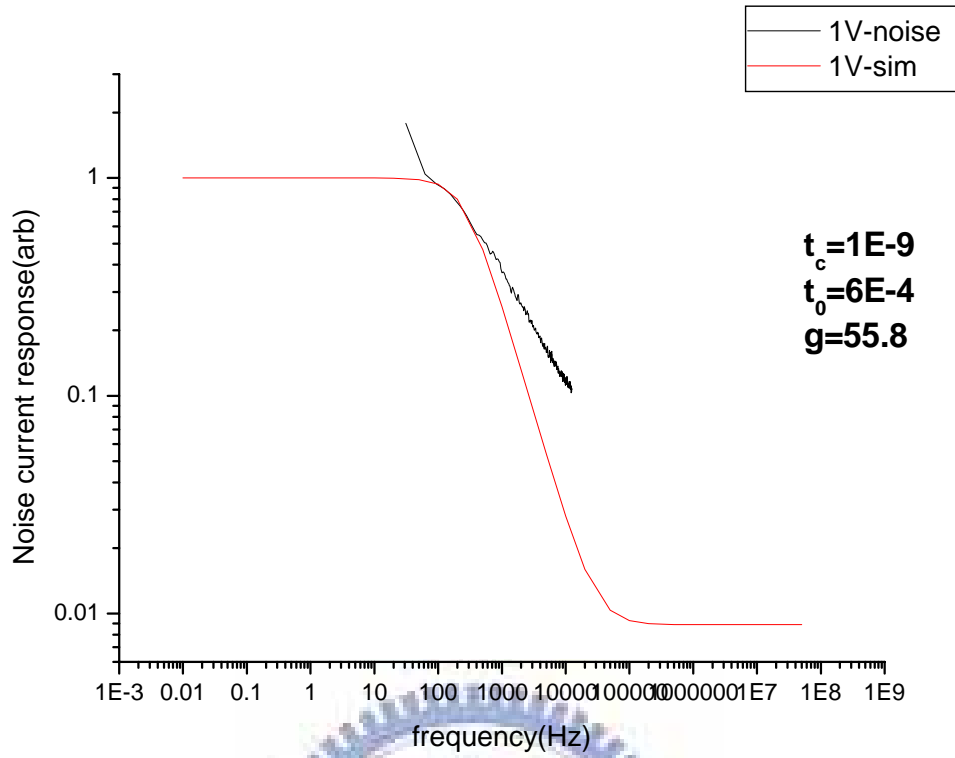


Fig 5-11 The noise fitting at 60K

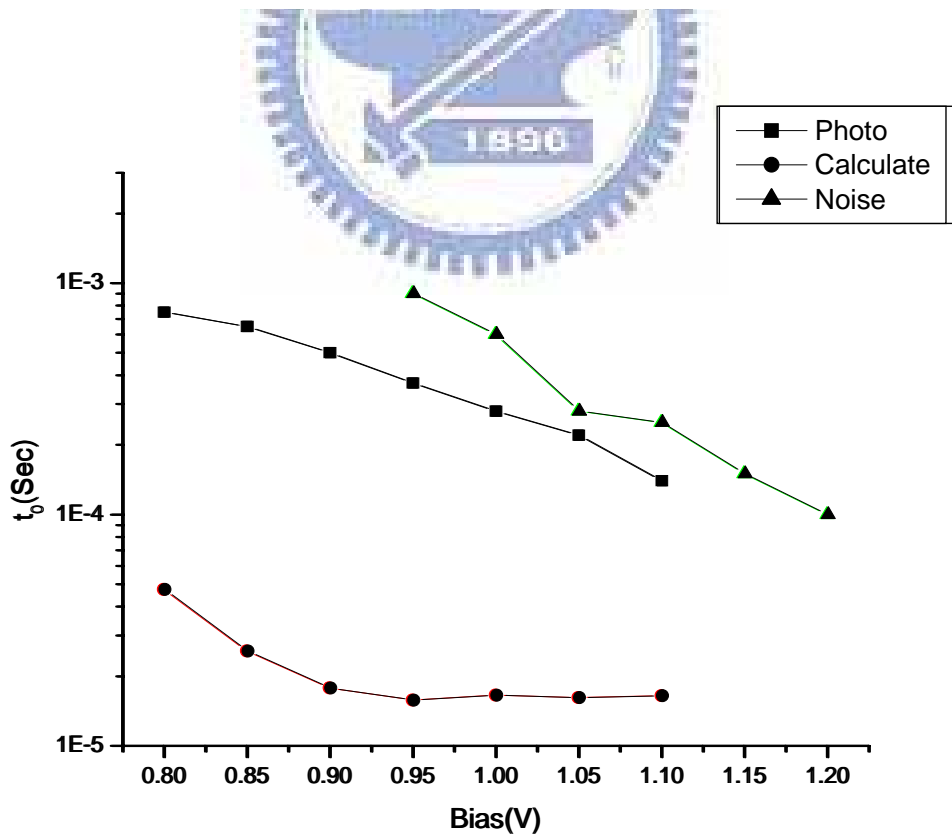


Fig 5-12(a) τ_o fitting at 60K

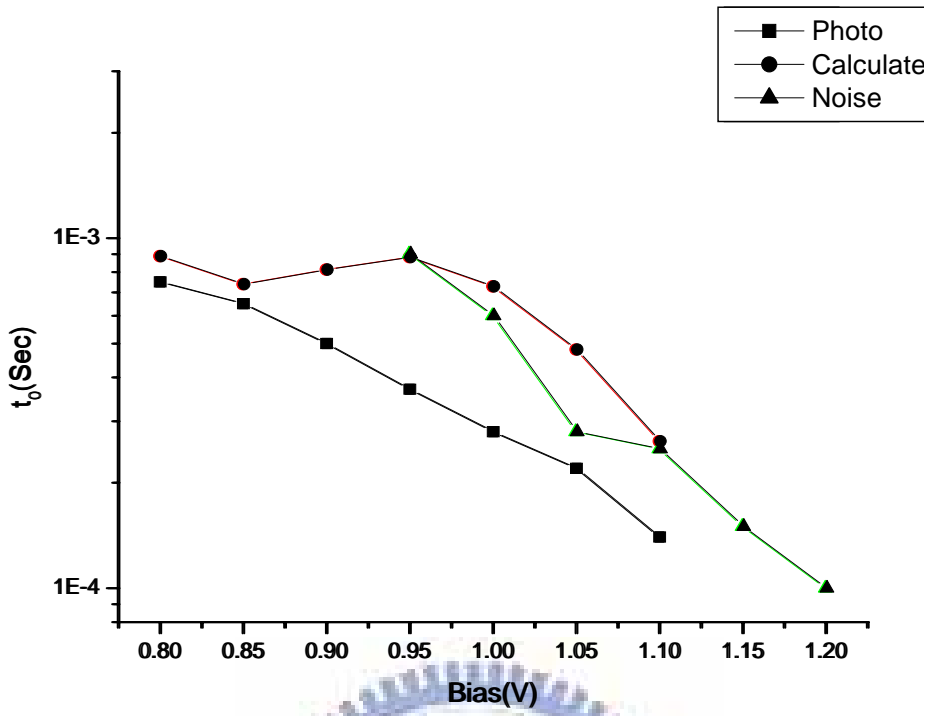


Fig 5-12(b) τ_0 fitting after calibration

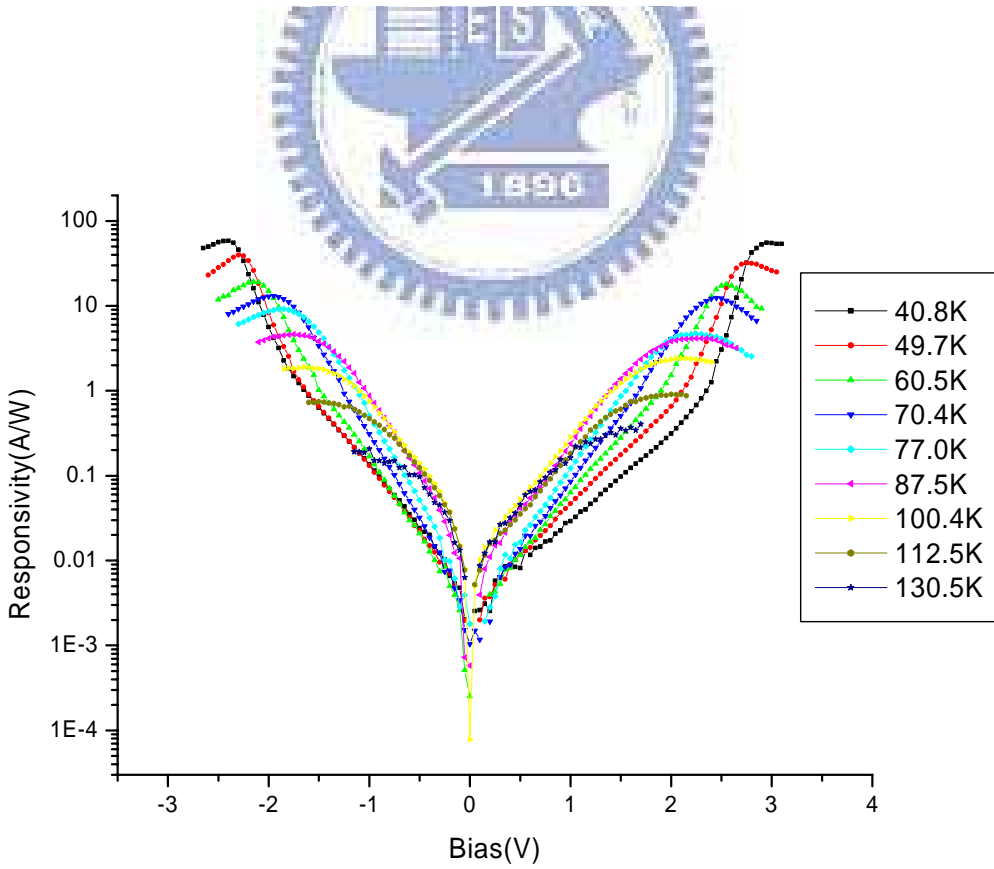


Fig 5-13 The peak responsivity of sample B

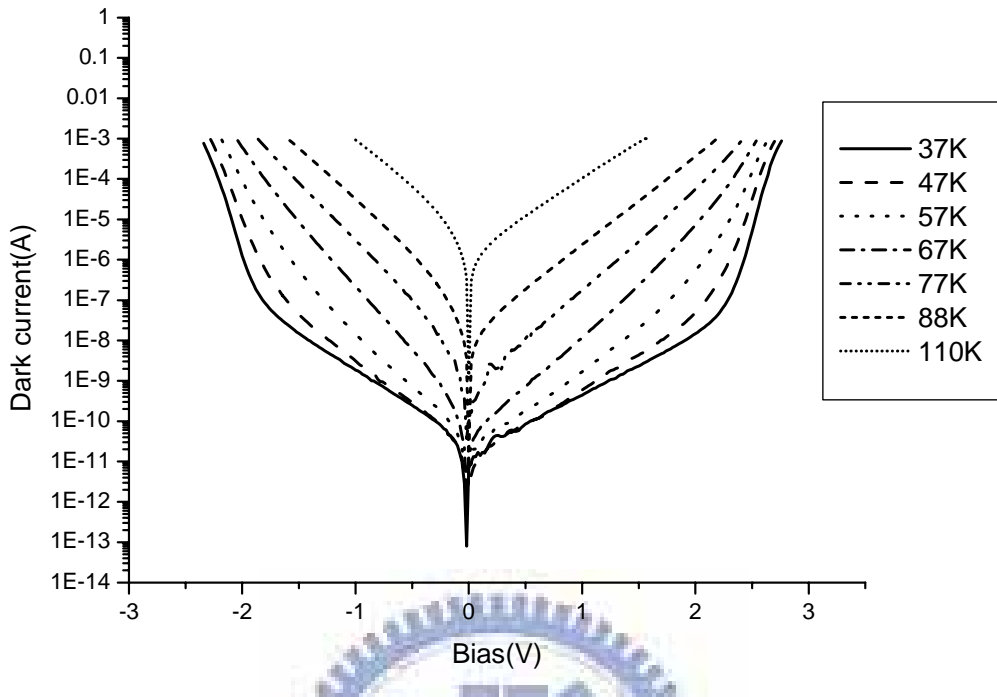


Fig 5-14 Dark currents for different temperature

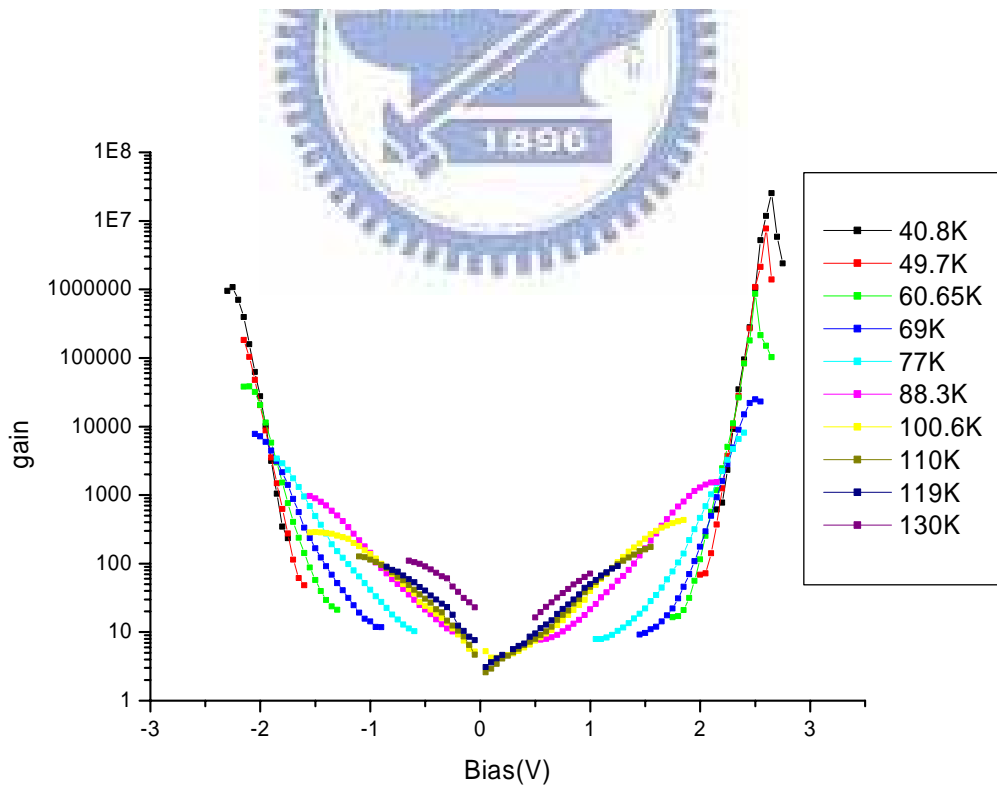


Fig 5-15 The noise gain g_n for different temperature

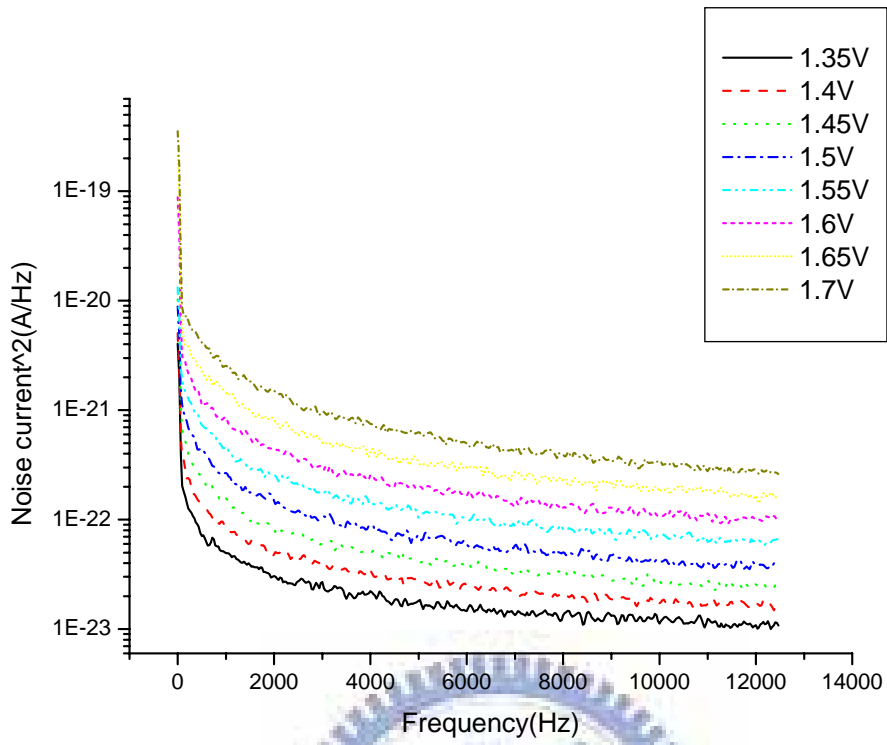


Fig 5-16 Noise current at 77K

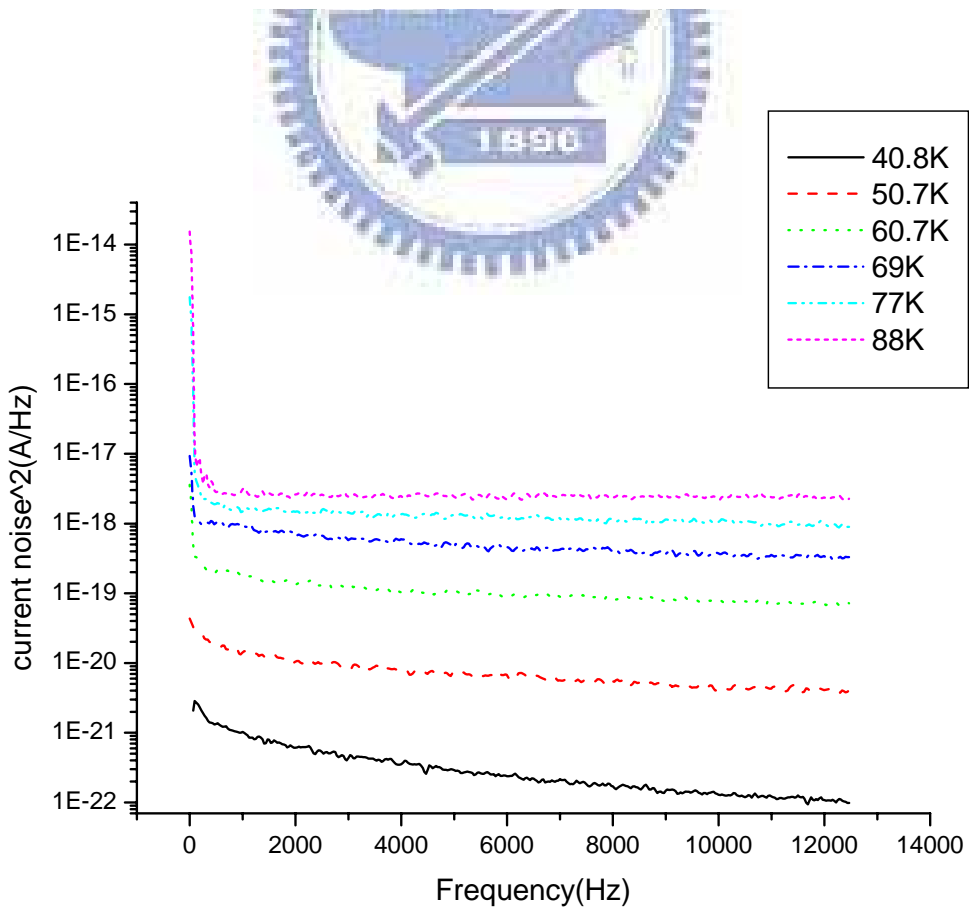


Fig 5-17 Noise current at 2.3V

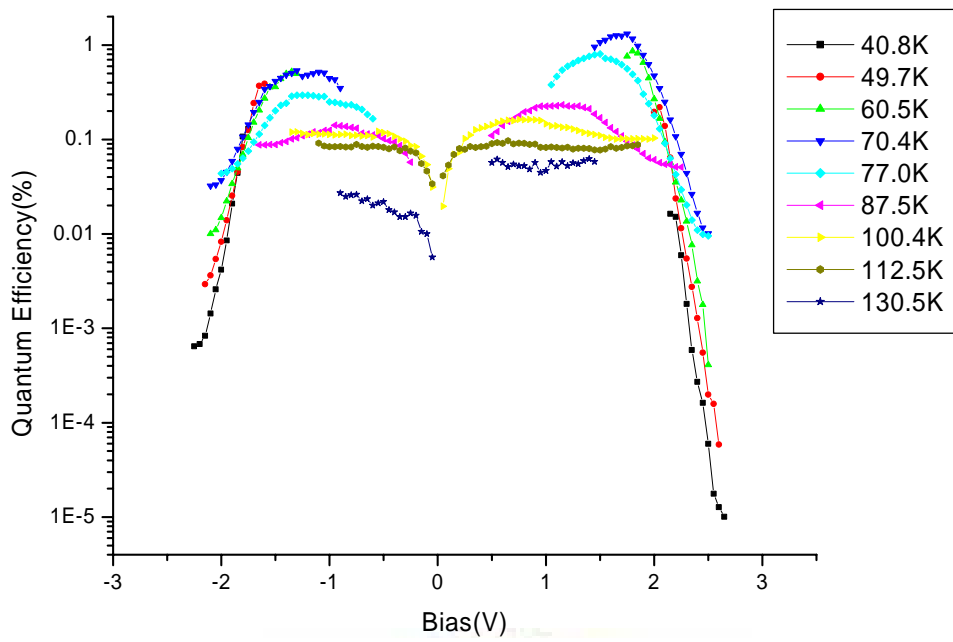


Fig 5-18 The ratio of responsivity to the noise gain



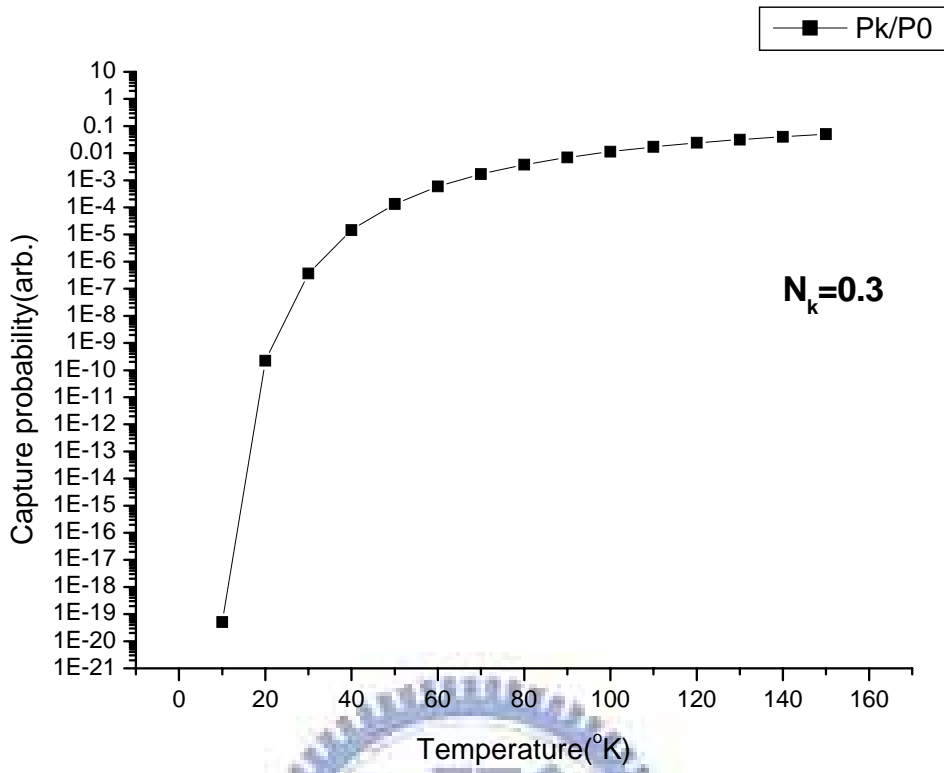


Fig 5-19(a) Capture probability when $N_k=0.3$

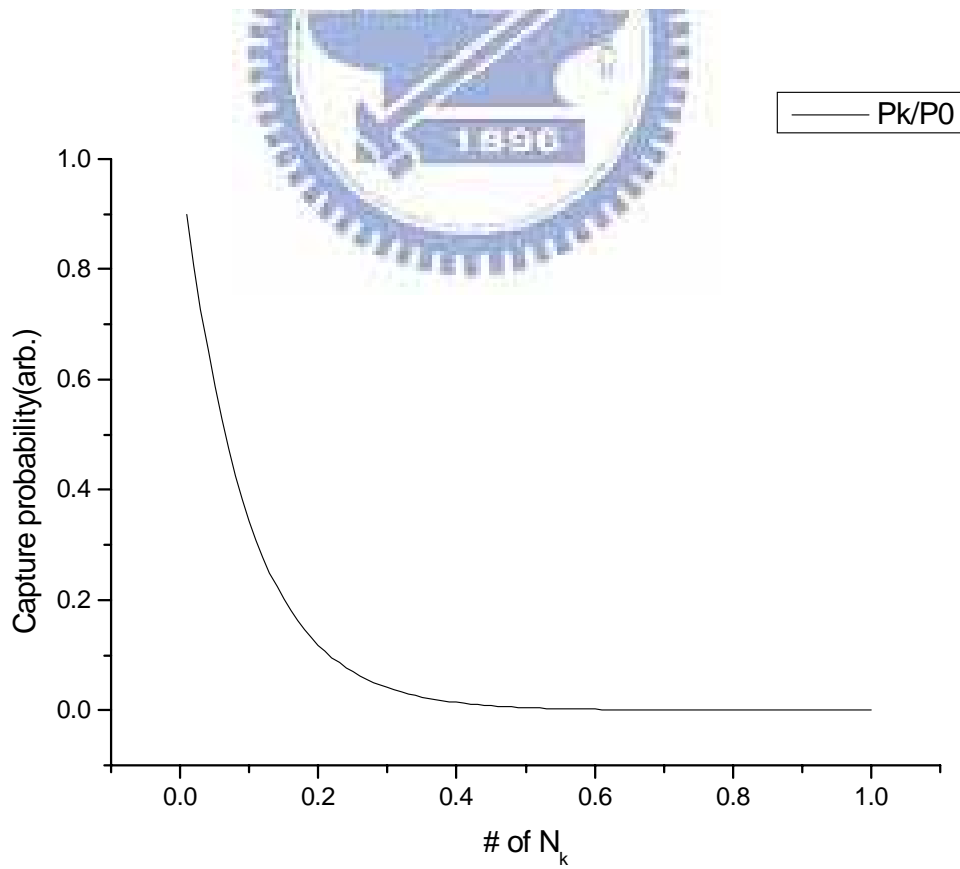


Fig 5-19(b) Capture probability

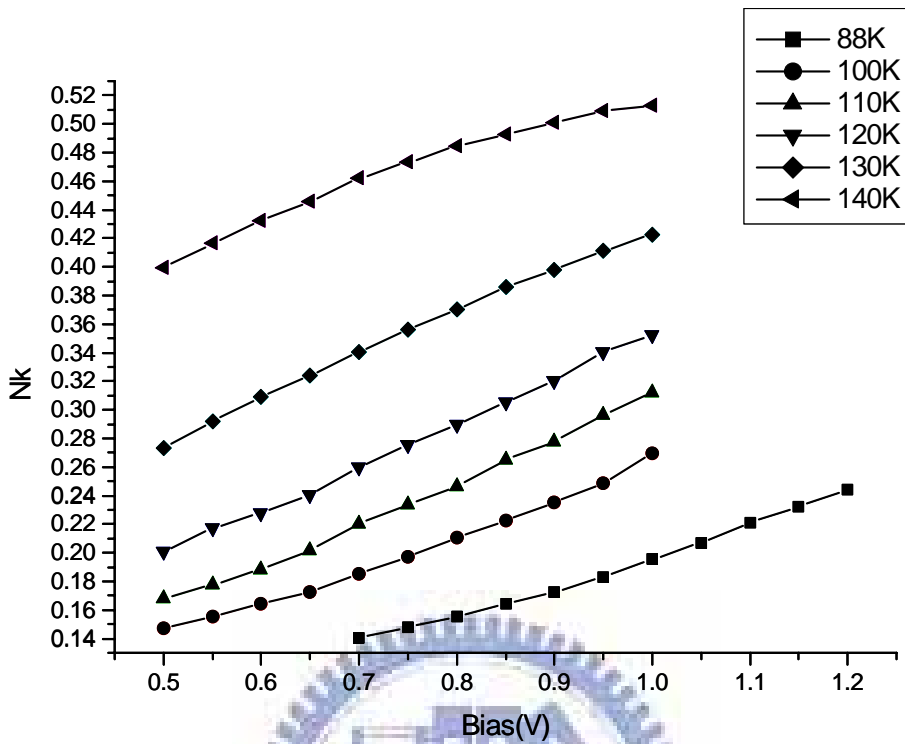


Fig 5-20 N_k for difference bias and temperature of sample B

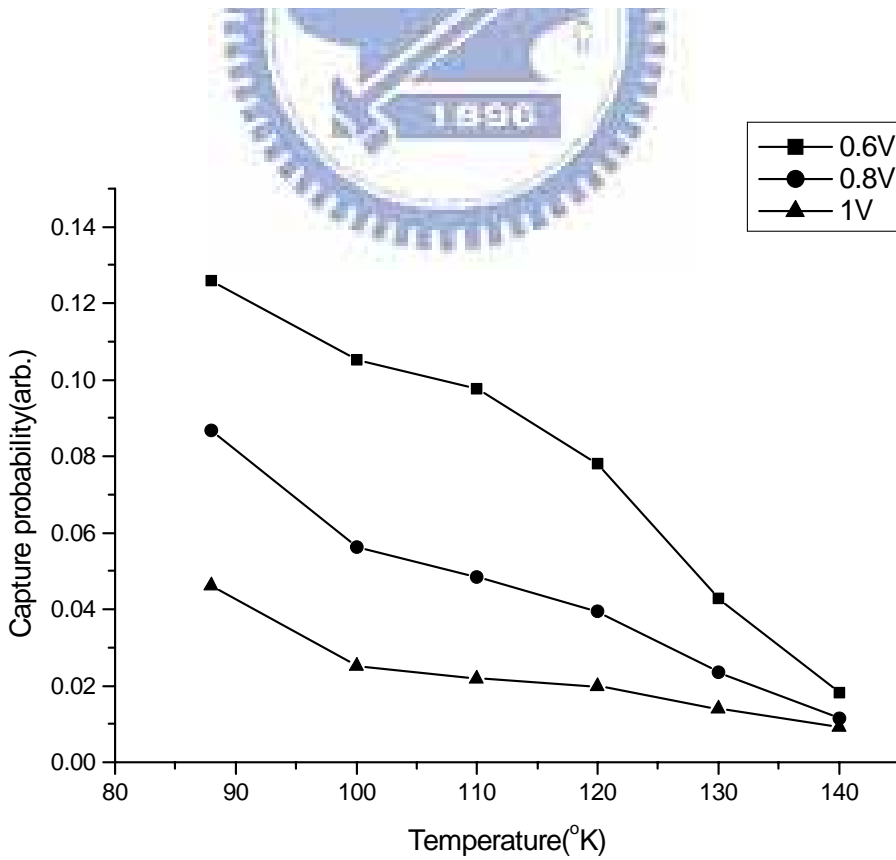


Fig 5-21 Capture probability ($1/g$) for different bias

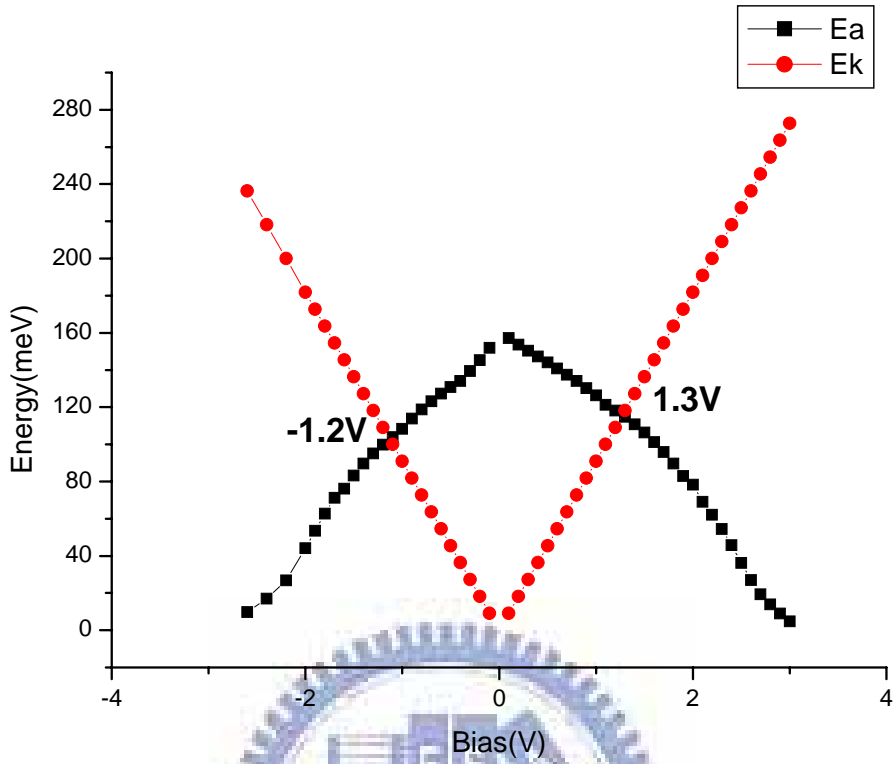


Fig 5-22 Activation energy and kinetic Energy

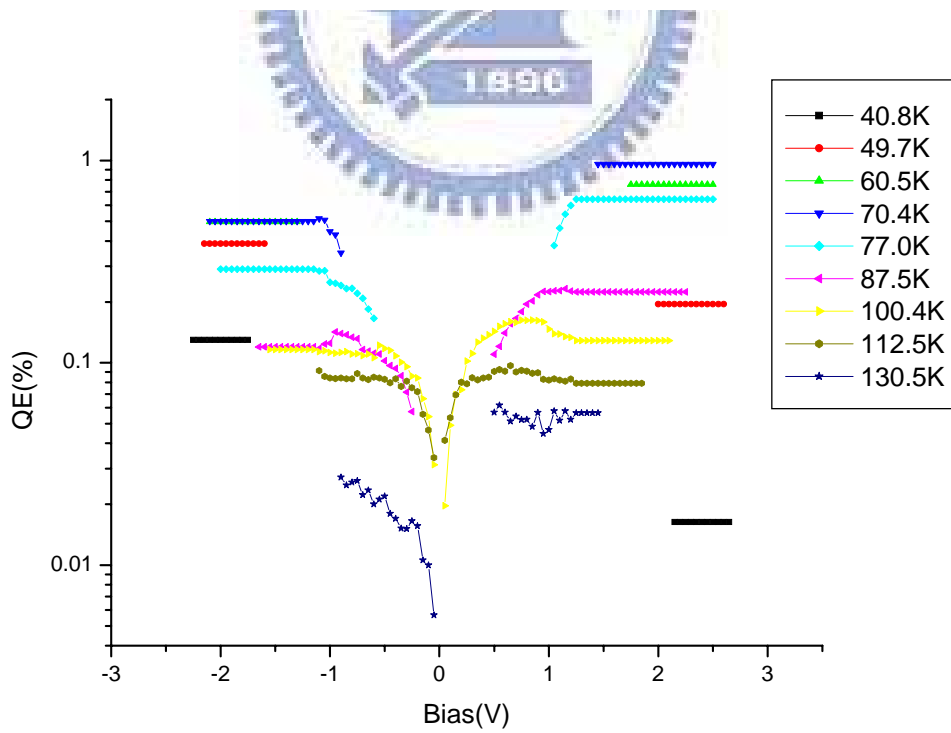


Fig 5-23 Quantum efficiency

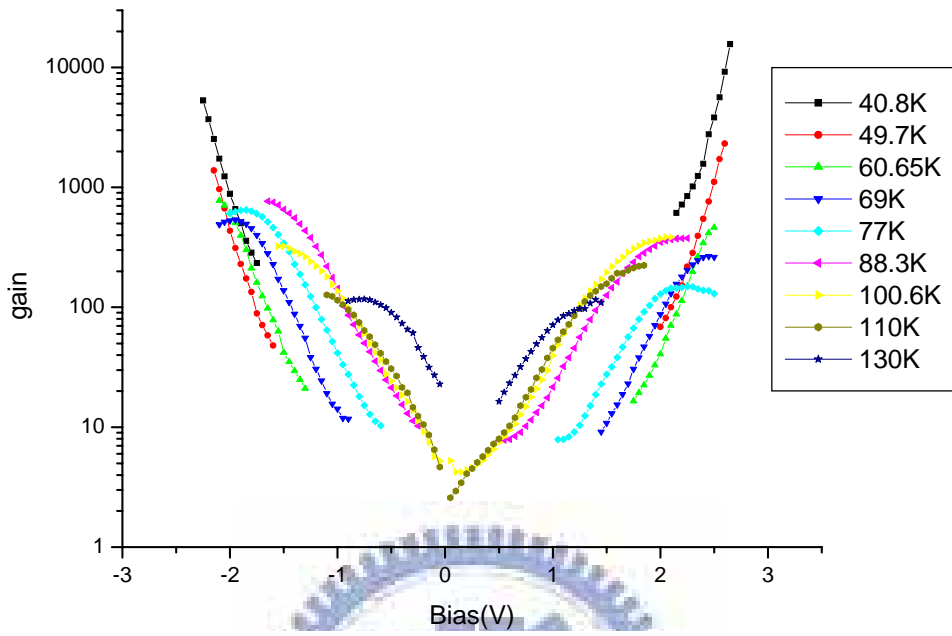


Fig 5-24 photo response gain g_{ph}

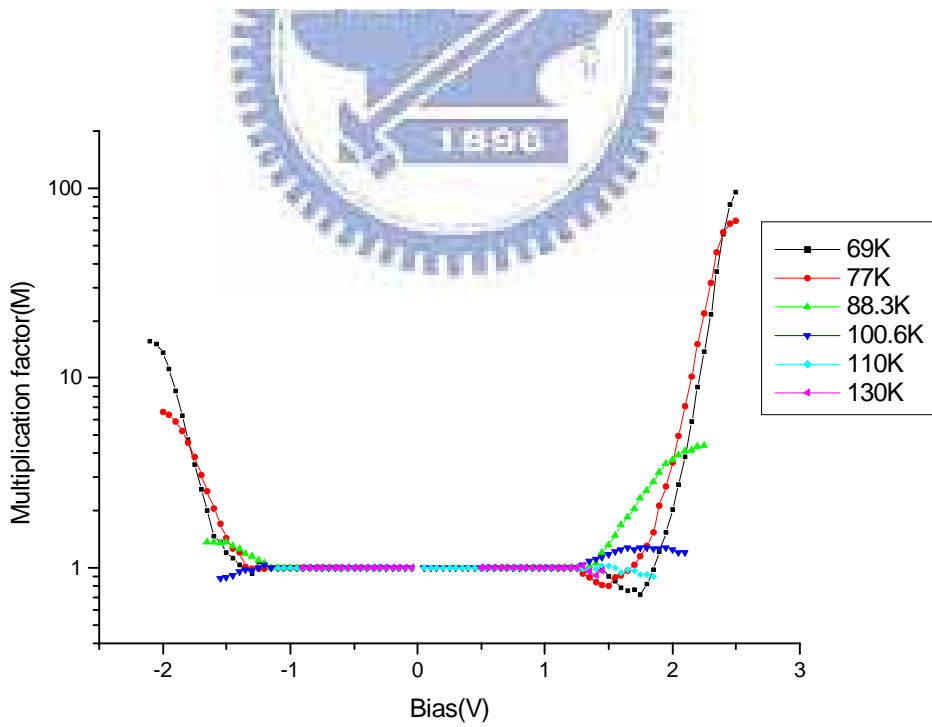


Fig 5-25 Multiplication factor

Reference

- [1] B. F. Levine, "Quantum-Well Infrared Photodetectors," *J. Appl. Phys.*, vol. 74, pp. R1-R81, 1993.
- [2] John E. Hubbs, Douglas C. Arrington, Mark E. Gramer, Gary A. Dole "Nonlinear response of quantum well infrared photodetectors under low-background and low-temperature conditions", *Opt.Eng*, vol. 39, pp.2660-2671, Oct. 2000.
- [3] Adrienne D. Stiff, Sanjay Drishna, Pallab Bhattacharya, and Stephen W. Keenerly, "Normal-Incidence, High-Temperature, Mid-Infrared, InAs-GaAs Vertical Quantum-Dot Infrared Photodetector," *IEEE J Quantum Electronics*, vol. 37, pp. 1272-1279, 2001.
- [4] S. Y. Wang, S. D. Lin, H. W. Wu, and C. P. Lee, "Low Dark Current Quantum Dot Infrared Photodetectors with AlGaAs Current Blocking Layer," *Appl. Phys. Lett.*, vol. 78, pp. 1023-1025, Feb. 2001.
- [5] D. Pan, E. Towe, and S. Kennerly, "Normal-incident intersubband (In, Ga)As/GaAs quantum dot infrared photodetectors," *Appl. Phys. Lett.*, vol. 73, pp. 1937-1939, Oct. 1998.
- [6] V. Ryzhii, V. Pipa, I. Khmyrova, V. Mitin, M. Willander, W. Magnus., "Dark Current in Quantum Dot Infrared Photodetectors", *J. J. Appl*, vol. 39. pp. 1283-1285.
- [7] M. Ershov, S. Satou, Y. Ikebe, "Analytical Model of Transient Photoresponse of Quantum Well Infrared Photodetectors" *J. Appl. Phys.* vol. 86, pp. 6442-6450, Dec 1999.
- [8] H. Schneider, "Theory of Avalanche Multiplication and Excess Noise in Quantum-Well Infrared Photodetectors", *Appl. Phys.* vol.82, pp. 4376-4378, Jun 2003.
- [9] K. K. Choi, "The Physics of Quantum Well Infrared Photodetectors," *World Scientific*.
- [10] Elias Towe and Dong Pan, "Semiconductor Quantum-Dot Nanostructures: Their Application in a New Class of Infrared Photodetectors," *IEEE J Selected Topics in Quantum Electronics*, vol. 6, pp. 408-419, 2000.
- [11] Shun Lien Chuang, "Physics of Optoelectronic Devices," *John Wiley & Sons, Inc.*
- [12] Werner Seifert, Niclas Carsson, Mark Miller, Mats-Erik Pistol, Lars Samuelson and L. Reine Wallenberg, "In-situ Growth of Quantum Dot Structures by the Stranski-Krastanow Growth Mode," *Prog. Crystal Growth and Charat.* Vol. 33, pp. 423-471, 1996.
- [13] John David Vincent, "Fundamentals of Infrared Detector Operation and Testing,"

John Wiley & Sons, Inc.



簡歷(Vita)

姓名: 黃博聲(Po-sheng Huang)

出生年月日: 民國 69 年 9 月 27 日

籍貫: 台灣省台南市

學歷: 國立交通大學電子工程系 (87.9-91.6)

國立交通大學電子研究所碩士班(91.9-93.6)

碩士論文題目: 量子點紅外線偵測器之研究

The Studies of Quantum Dot Infrared Photodetectors

